Article

Observation of an ultra-high-energy cosmic neutrino with KM3NeT

https://doi.org/10.1038/s41586-024-08543-1

Received: 19 August 2024

Accepted: 18 December 2024

Published online: 12 February 2025

Open access

Check for updates

The KM3NeT Collaboration*✉

The detection of cosmic neutrinos with energies above a teraelectronvolt (TeV) offers a unique exploration into astrophysical phenomena[1–3]. Electrically neutral and interacting only by means of the weak interaction, neutrinos are not deflected by magnetic fields and are rarely absorbed by interstellar matter: their direction indicates that their cosmic origin might be from the farthest reaches of the Universe. High-energy neutrinos can be produced when ultra-relativistic cosmic-ray protons or nuclei interact with other matter or photons, and their observation could be a signature of these processes. Here we report an exceptionally high-energy event observed by KM3NeT, the deep-sea neutrino telescope in the Mediterranean Sea[4], which we associate with a cosmic neutrino detection. We detect a muon with an estimated energy of 120^{+110}_{-60} petaelectronvolts (PeV). In light of its enormous energy and near-horizontal direction, the muon most probably originated from the interaction of a neutrino of even higher energy in the vicinity of the detector. The cosmic neutrino energy spectrum measured up to now[5–7] falls steeply with energy. However, the energy of this event is much larger than that of any neutrino detected so far. This suggests that the neutrino may have originated in a different cosmic accelerator than the lower-energy neutrinos, or this may be the first detection of a cosmogenic neutrino[8], resulting from the interactions of ultra-high-energy cosmic rays with background photons in the Universe.

Cosmic neutrinos may be produced either in the vicinity of the cosmic-ray source or along the cosmic-ray propagation path, leading to the production of secondary unstable particles, which subsequently decay into neutrinos. Cosmic rays interacting in the Earth's atmosphere produce atmospheric neutrinos, which form an experimental background to cosmic neutrinos. To detect cosmic neutrinos, very-large-volume neutrino observatories monitor natural bodies of water or ice for the Cherenkov light induced by the passage of the charged particles that result from neutrino interactions in or near the detector. The KM3NeT research infrastructure comprises two detector arrays of optical sensors deep in the Mediterranean Sea[4]. The ARCA detector is located offshore Portopalo di Capo Passero, Sicily, Italy, at a depth of about 3,450 m and connected by means of an electro-optical cable to the shore station of the INFN, Laboratori Nazionali del Sud (LNS). The geometry of ARCA is optimized for the study of high-energy cosmic neutrinos. The ORCA detector is located at a depth of about 2,450 m, offshore Toulon, France, and is optimized for the study of neutrino oscillations. Both detectors are under construction but already operational. Once completed, they will comprise 345 (230 for ARCA and 115 for ORCA) vertical detection lines, each holding 18 optical modules. Each module hosts 31 3-inch photomultiplier tubes (PMTs) pointing in all directions and ensuring 4π coverage[9]. Both detectors can identify all flavours of neutrino interactions: those producing long-lived muons, denominated 'tracks', and those producing electromagnetic and hadronic cascades at the neutrino interaction vertex, denominated 'showers'.

Of interest in this article are neutrino interactions that produce high-energy muons, which can travel several kilometres in seawater before being absorbed. These muons lose energy as they propagate mainly because of stochastic radiative processes such as bremsstrahlung, pair production and photonuclear reactions. The average energy loss per unit path length is proportional to the muon energy. Electromagnetic cascades arise from these stochastic energy losses; the number of charged particles that produce Cherenkov radiation in the cascades is proportional to the amount of energy lost by the muon in the process. The recorded time of arrival and time-over-threshold of the signals on the PMTs (denoted as 'hits') are used to reconstruct the muon direction and energy.

Although atmospheric neutrinos are more abundant at lower energies (≈TeV), cosmic neutrinos should become dominant at energies above 100 TeV. The neutrino energy is thus a crucial parameter for establishing a cosmic origin. The IceCube Collaboration announced the discovery of PeV cosmic neutrinos in 2013 (ref. 10). The most energetic neutrinos reported so far are a 6.05 ± 0.72 PeV electron antineutrino observed at the energy of the Glashow resonance[11] and a muon neutrino above 10 PeV from the observation of a 4.4-PeV muon[5].

The neutrino event KM3-230213A

An extremely high-energy muon traversing the ARCA detector was observed on 13 February 2023 at 01:16:47 UTC. This event is referred to here as KM3-230213A. At that time, 21 detection lines were in operation.

*A list of authors and their affiliations appears at the end of the paper. ✉e-mail: km3net-pc@km3net.de

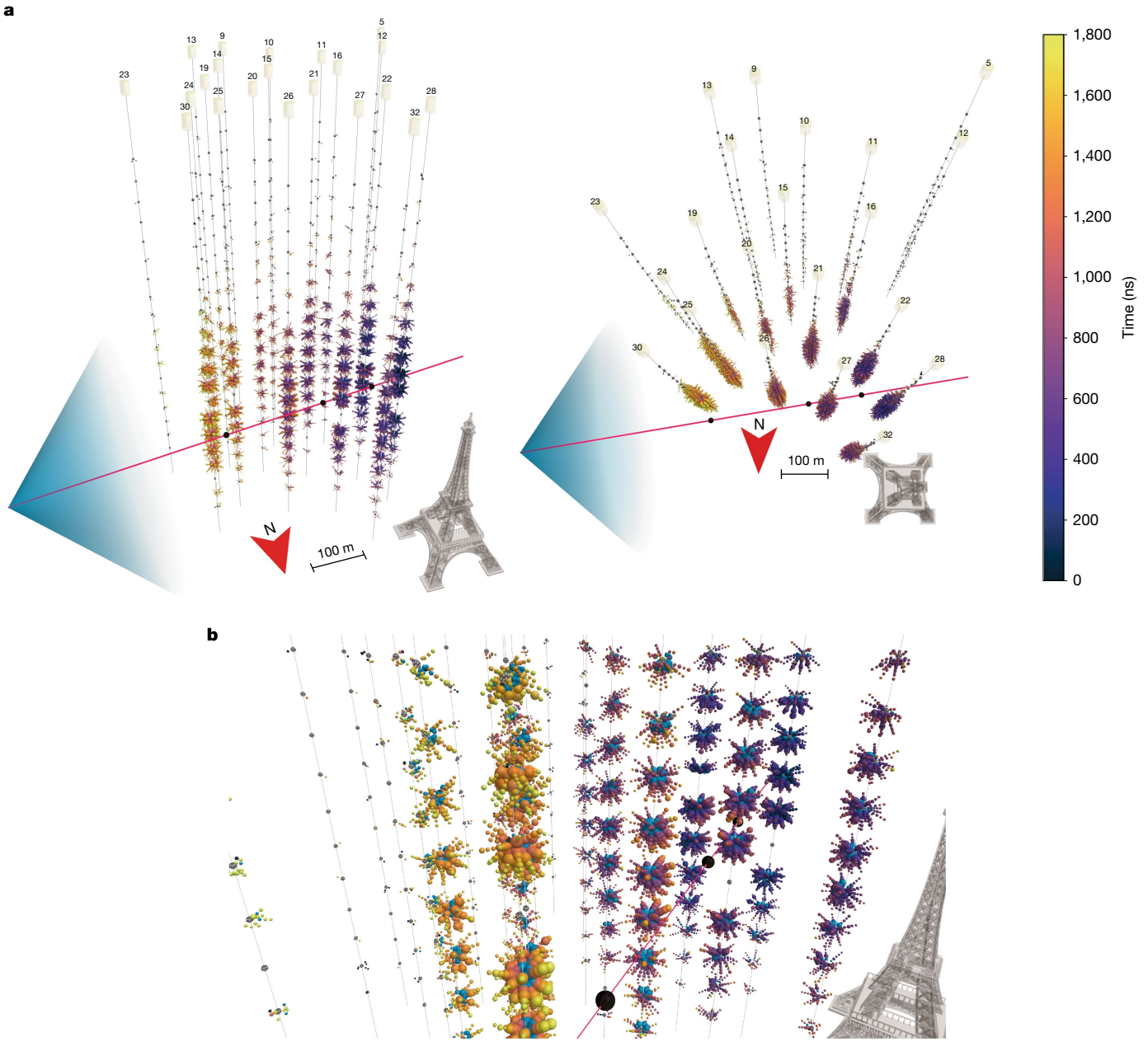

Fig. 1 | Views of the event. a, Side and top views of the event. The reconstructed trajectory of the muon is shown as a red line, along with an artist's representation of the Cherenkov light cone. The hits of individual PMTs are represented by spheres stacked along the direction of the PMT orientations. Only the first five hits on each PMT are shown. As indicated in the legend, the spheres are coloured according to the detection time relative to the first triggered hit. The size of the spheres is proportional to the number of photons detected by the corresponding PMT. The locations of the secondary cascades, discussed in the Supplementary Material, are indicated by the black spheres along the muon trajectory. The north direction is indicated by a red arrow. A 100-m scale and the Eiffel Tower (330 m height, 125 m base width) are shown for size comparison. **b**, Zoomed-in view of the optical modules that are close to the first two observed secondary showers in the event. Here light-blue spheres represent hits that arrive within −5 to 25 ns of the expected Cherenkov arrival times.

The detector was in this configuration from 23 September 2022 until 11 September 2023, when seven further lines were installed. After removing data acquired in the detector commissioning phase and during detector calibration periods, 287.4 days of data taking were selected for analysis with this configuration. During this period, about 110 million events were triggered and KM3-230213A is the highest-energy event observed. KM3-230213A is visualized in Fig. 1. A total of 28,086 hits were registered by the 21 detection lines. Owing to the large amount of detected light, the PMTs closest to the muon trajectory are saturated. As expected for very-high-energy muons, at least three large showers, probably because of energy-loss processes, are observed along the track (more details are provided in the Supplementary Materials).

The muon trajectory is reconstructed from the measured times and positions of the first hits recorded on the PMTs, using a maximum-likelihood algorithm, described in Methods. KM3-230213A is the event with the best track log-likelihood among all those collected in this detector configuration, indicative of a highly relativistic muon travelling several hundreds of metres through the detector. The direction of KM3-230213A is reconstructed as near-horizontal, originating 0.6° above the horizon at an azimuth of 259.8° (azimuth angles increase clockwise, with north at 0°). The uncertainty on the direction is estimated to be 1.5° (68% confidence level), dominated by the present systematic uncertainty on the absolute orientation of the detector. The origin of this uncertainty is described in Methods. A dedicated sea campaign

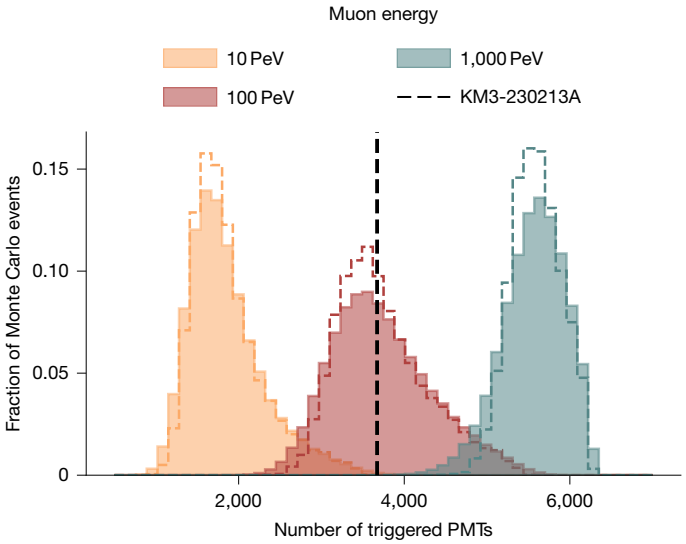

Fig. 2 | Number of PMTs in the event. The normalized distributions of the number of PMTs participating in the triggering of the event for simulated muon energies of 10, 100 and 1,000 PeV. The vertical dashed line indicates the observed value in KM3-230213A, $\hat{\mathcal{N}}_{\mathrm{trig}}^{\mathrm{PMT}} = 3{,}672$. The dashed histograms represent the distributions from the nominal simulations, whereas, in the filled histograms, systematic uncertainties are included by weighting the simulations according to a normal distribution, centred at the nominal value of the nuisance parameter and with a ±10% uncertainty. At the highest energy, the distributions seem to be truncated around $\mathcal{N}_{\mathrm{trig}}^{\mathrm{PMT}} = 6{,}000$ because the track crosses the detector in its periphery.

is planned in the future to improve the knowledge of the positions of the detector elements on the seafloor; a recalibration of all data will then be performed and will allow us to approach the intrinsic statistical uncertainty on the muon direction of 0.12° (median, as described in Methods).

The muon energy at the detector is estimated by counting the number of PMTs that participate in the triggering of the event, $\mathcal{N}_{\mathrm{trig}}^{\mathrm{PMT}}$. This quantity is robust against limitations of the detector simulations, as described in Methods, and against contamination from the optical backgrounds in seawater. The observed number of triggered PMTs for KM3-230213A is $\hat{\mathcal{N}}_{\mathrm{trig}}^{\mathrm{PMT}} = 3{,}672$, corresponding to about 35% of the active PMTs in the detector at the time of the event. This is much larger than for any other neutrino-induced event observed so far in the detector.

Distributions of $\mathcal{N}_{\mathrm{trig}}^{\mathrm{PMT}}$ as a function of the muon energy, for modelled muons arriving from the same position and direction of KM3-230213A, are obtained from Monte Carlo simulations. These are used to build frequentist confidence intervals[12,13] on the true muon energy, as described in Methods. Systematic uncertainties are included in the estimation by varying the simulated optical module efficiencies, and the scattering and absorption length of light, with respect to the nominal values. The $\mathcal{N}_{\mathrm{trig}}^{\mathrm{PMT}}$ distributions for simulations of 10-PeV, 100-PeV and 1,000-PeV muons are shown in Fig. 2. The estimated muon energy is 120^{+110}_{-60} PeV, with a 90% confidence level interval of 35–380 PeV. Uncertainties on the muon energy estimate are dominated by the knowledge of the absorption length of light in the seawater.

The considered range of variations for photon absorption (±10%) is derived from the observed variations of the water transparency in dedicated measurements[14]. Several studies in recent data have confirmed this. The number of first hits with small residuals (that is, compatible with a direct photon path from the track to the PMT) has been studied in KM3-230213A. At large distances, this number is sensitive to the absorption length. Data were found to be in the ±10% range obtained from simulations with modified absorption. A similar study was carried out using downgoing atmospheric muons, which also confirmed that deviations from nominal are at most on the order of 10%. Finally, the absorption can be determined from the observed rate of photons from radioactive ^{40}K in the seawater, which scales linearly with the absorption length. A first-principles computation[15] using the nominal absorption model predicts 5.1 ± 0.6 kHz, for which the uncertainty comes from the PMT efficiency and the number of photons created in the decay. The observed count rate is 5.6 kHz after accounting for dark noise and afterpulses, which is within the assigned 10% uncertainty range.

Figure 3 is an illustration of the position of KM3-230213A in the ($\mathcal{N}_{\mathrm{trig}}^{\mathrm{PMT}}$, cos(zenith angle)) phase space. Simulated Monte Carlo events are shown in Fig. 3a, with the expected annual rates of atmospheric muons[16] and cosmic neutrinos[5] in ARCA. The distribution for the ARCA data is shown in Fig. 3b, also highlighting KM3-230213A. Events are selected choosing well-reconstructed tracks, as defined on the basis of the observed track length in the detector (track length larger than 250 m) and the track reconstruction likelihood: log-likelihood ratio larger than 500, selecting 0.02% of all reconstructed atmospheric muon and neutrino tracks and 2% of the cosmic tracks assuming the flux from ref. 5.

Given the reconstructed energy and direction, an upper limit on the background of atmospheric muons is estimated using dedicated simulations, as described in Methods. A muon with the observed direction would have traversed about 300 km water-equivalent of material, which exceeds the maximal range of any atmospheric muon (≤60 km water-equivalent for 100-EeV muons). The upper limit on the muon contamination at 100 PeV, considering an error on the zenith angle estimate as large as 2°, is 10^{-10} events per year. This number becomes on the order of 10^{-9} events per year if the muon energy is instead 10 PeV. In the very unlikely scenario that the detector is misaligned and the true zenith angle would deviate by 5σ from nominal (that is, arrival direction 5.6° above the horizon), muons would need to travel through 28 km water-equivalent and the upper limit on the rate becomes 10^{-4} muons per year and 10^{-3} for muon bundles in which several parallel muons from the same cosmic-ray air shower could reach the detector.

Atmospheric neutrinos could reach the detector, but their number decreases substantially above PeV energies. The expected rate of atmospheric neutrinos above 100 PeV is on the order of $(1–5) \times 10^{-5}$ events per year, dominated by the prompt atmospheric component owing to the decay of short-lived hadrons from cosmic-ray interactions in the atmosphere. The probability that KM3-230213A is of cosmic origin is much greater than any hypothesis involving an atmospheric origin, and various estimations are provided in Methods and Supplementary Materials. Beyond Standard Model hypotheses on its origin have not been investigated here.

The measured muon energy serves as a lower limit on the incoming neutrino energy. Given the estimated muon energy and its uncertainty, the median neutrino energy that produces such muons in the simulations of the ARCA detector is 220 PeV; 68% (90%) of simulated events from the whole sky fall in the 110–790 PeV (72 PeV–2.6 EeV) energy range, under the assumption that the incoming neutrino energy spectrum is $\propto E_\nu^{-2}$.

An isotropic flux of neutrinos at ultra-high energies would give rise to events detected near the horizon: downgoing neutrinos are hidden in an overwhelming background of atmospheric muons, whereas the upgoing neutrino flux is severely suppressed, because neutrinos of such large energies would interact in the Earth. The arrival direction of KM3-230213A matches this scenario.

Celestial origin

The equatorial coordinates (J2000) and the detection time of KM3-230213A are: RA = 94.3°, dec. = −7.8°, MJD = 59988.0533299. The different containment radii are: R(50%) = 1.2°, R(68%) = 1.5°, R(90%) = 2.2° and R(99%) = 3.0°, dominated by the systematic uncertainty on the absolute orientation of the detector (see Methods). The celestial position of KM3-230213A is shown in Fig. 4, together with the different error region

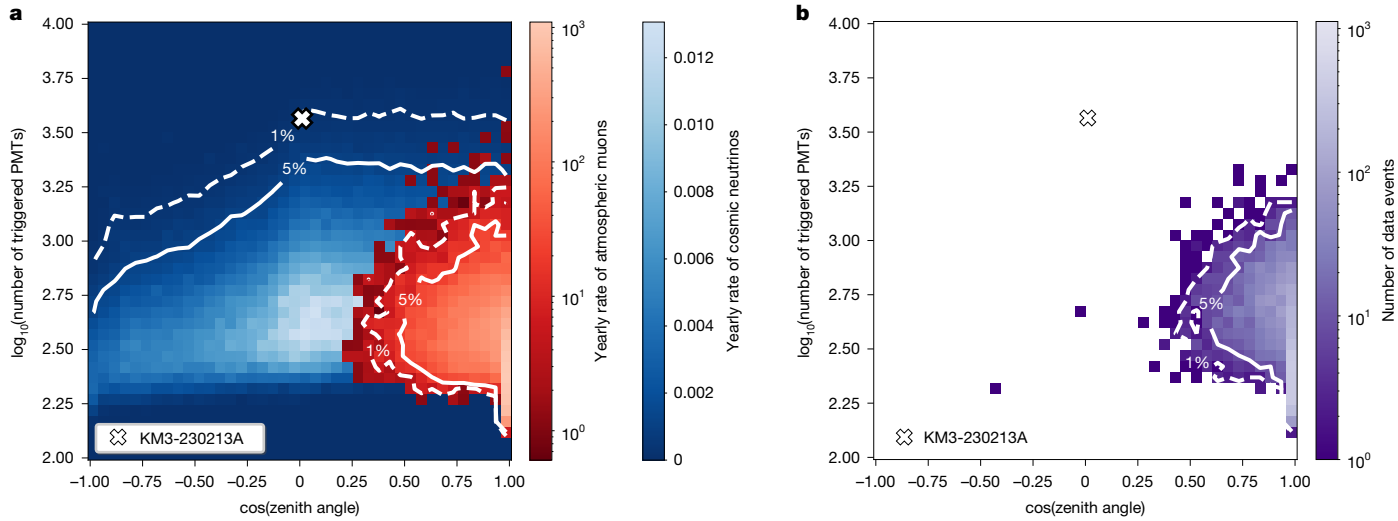

Fig. 3 | Background rates. a, Expected yearly rate of atmospheric muons and cosmic neutrinos (according to the best-fit flux of ref. 5) in ARCA per bin of $\mathcal{N}_{\mathrm{trig}}^{\mathrm{PMT}}$ and cos(zenith angle). The solid (dashed) lines mark the boundary of the phase space outside which 5% (1%) of the muon and neutrino distributions are contained. KM3-230213A is shown by the cross. **b**, Number of events collected in the ARCA detector over the 287 days of data taking with 21 detection lines, with the same selection cuts. Two upgoing, lower-energy events are visible as well as KM3-230213A, which are candidate neutrino events, subject to future analysis.

contours. Searches were performed for a potential source counterpart within a 3° radius around the event coordinates with publicly available multiwavelength data. Four hypotheses were tested: galactic, local Universe, transient and extragalactic origin.

As the direction of the event is compatible with the extension of the galactic interstellar medium (about 10° above and below the galactic plane), galactic counterpart was searched for in high-energy (4FGL-DR4 (ref. 17)) and very-high-energy (TeVCat[18]) gamma-ray catalogues, as well as in the 3HWC survey data[19]. Despite the presence of the Orion molecular clouds in the error region, no catalogued source was found in the 99% error region. The direction of the event was cross-matched with the MANGROVE catalogue[20] for distances up to 100 Mpc to explore a local origin: 40 galaxies were found. For each galaxy, optical transient sources were searched for in the ZTF public stream in a ±6-month time window, using the FINK broker[21]. No transient source was identified. Also, no coincident detection of transient objects (such as gamma-ray bursts, tidal-disruption events, supernovae) was found in the GCN notices and circulars (https://gcn.nasa.gov/), in the Astronomer's Telegram (https://astronomerstelegram.org/) and in the Transient Name Server (https://www.wis-tns.org/).

Extragalactic neutrino sources should be dominated by active galactic nuclei, and blazars are of particular interest considering the very-high energy of KM3-230213A. To compile a census of potential blazar counterparts within the 99% confidence region of KM3-230213A, archival multiwavelength data were also explored. The following catalogues were cross-matched to investigate a possible blazar counterpart: the 4FGL-DR4 Fermi-LAT gamma-ray catalogue[17], the first eROSITA X-ray catalogue[22], the Wide-field Infrared Survey Explorer (WISE) optical catalogue[23], the RFC 2024b (https://astrogeo.org/rfc/) and NRAO VLA Sky Survey (NVSS)[24] radio catalogues and Roma-BZCAT[25]. Four different strategies were pursued, leading to a total of 12 objects. The selection criteria are described in Methods, together with the properties of these sources. The celestial positions of the selected sources are shown in Fig. 4. Given the large number of blazars in the sky, none of these associations can be considered compelling so far, and further investigations will be needed.

Given that a hypothetical astrophysical source associated with KM3-230213A may have also produced lower-energy neutrinos, data from the ARCA and ORCA detectors, as well as public data from the ANTARES and IceCube detectors, were checked for the presence of a neutrino signal compatible with a point-like source hypothesis in the vicinity of KM3-230213A. Details on the datasets, search approaches and results are given in Methods. The largest excess was found in the IceCube data at a distance of 2.4° from KM3-230213A with a pre-trial *P*-value of 1.6×10^{-4} and a post-trial *P*-value of 0.07. No significant excess was

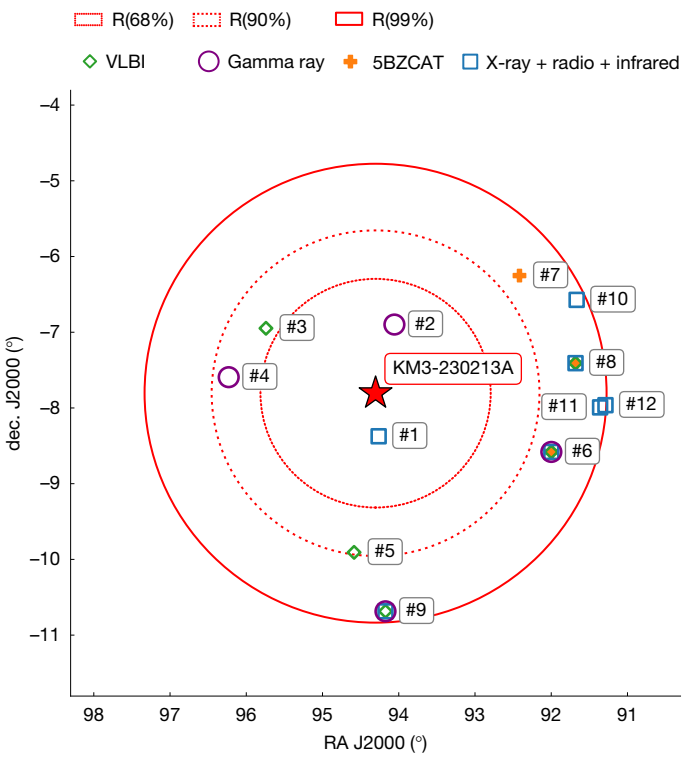

Fig. 4 | Sky map in the direction of KM3-230213A. KM3-230213A is indicated by the red star, with the error regions within R(68%), R(90%) and R(99%) shown as dotted, dashed and solid contours, respectively. The directions of the selected source candidates are shown as coloured markers, whose colours and marker type indicate the criterion according to which the source was selected. The sources are numbered according to their proximity to KM3-230213A, as reported in Methods.

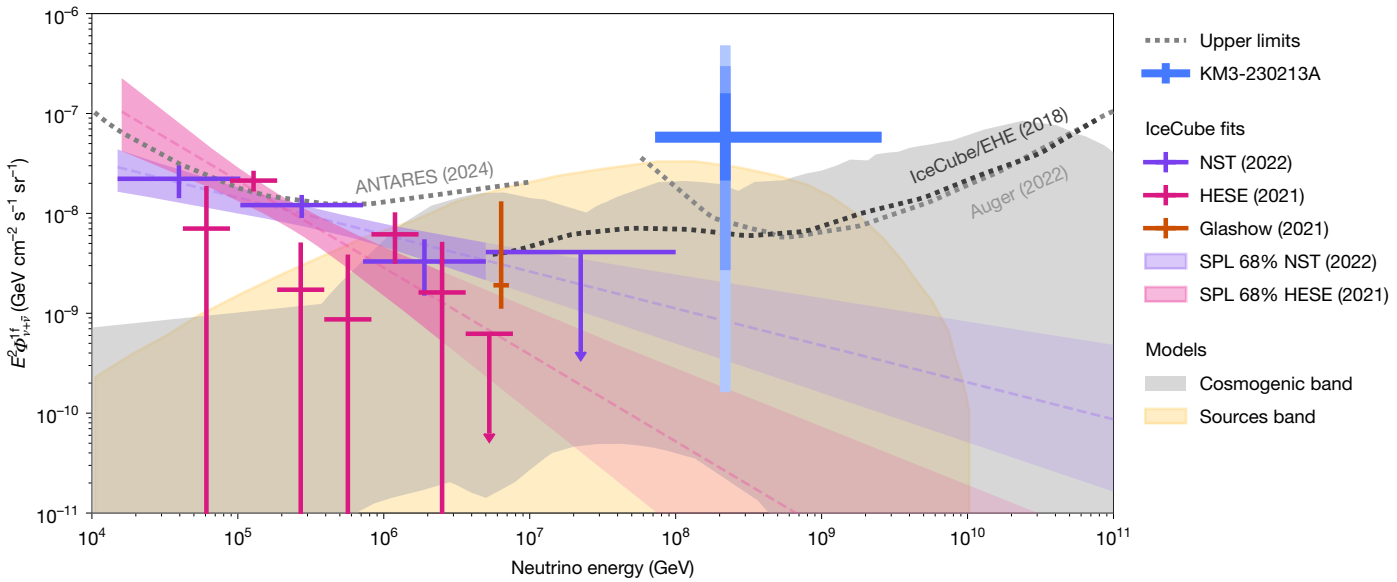

Fig. 5 | Comparison with models and earlier measurements. Shown is the energy-squared per-flavour astrophysical flux derived from the observation of KM3-230213A with measurements and theoretical predictions, assuming equipartition (ν_e:ν_μ:ν_τ = 1:1:1). The blue cross corresponds to the flux needed to achieve one expected event after the track selection described in the text, in the central 90% neutrino energy range associated with KM3-230213A, illustrated with the horizontal span; the vertical bars represent the 1σ, 2σ and 3σ Feldman–Cousins confidence intervals on this estimate. The purple and pink shaded regions represent the 68% confidence level contours of the IceCube single-power-law (SPL) fits (Northern Sky Tracks, NST[5]) and High-Energy Starting Events (HESE)[7], respectively: the darker-shaded regions are the respective 90% central energy range at the best fit (dashed line), whereas the lighter-shaded regions are extrapolations to higher energies. The purple and pink crosses are the piece-wise fit from the same analyses, whereas the orange cross corresponds to the IceCube Glashow resonance event[11]. The dotted lines are upper limits from ANTARES (95% confidence level[47]), Pierre Auger (90% confidence level, for an E^{-2} neutrino spectrum[28], corrected to convert from limits in half-decade to one-decade bins) and IceCube (90% confidence level, estimated assuming an E^{-1} neutrino spectrum in sliding one-decade bins[27]). The grey-shaded band comprises a variety of cosmogenic neutrino expectations following several models of cosmic-ray acceleration and propagation, whereas the yellow-shaded band comprises several scenarios of diffuse transient and variable extragalactic sources, both reported in the Supplementary Material.

observed at the coordinates of KM3-230213A and 90% confidence level upper limits on the one-flavour neutrino flux normalization at 1 GeV, $\Phi^{1\mathrm{GeV}}_{\nu+\bar{\nu}}$, assuming a neutrino spectrum of $\Phi_{\nu+\bar{\nu}}(E) = \Phi^{1\mathrm{GeV}}_{\nu+\bar{\nu}}(E(\mathrm{GeV}))^{-2}$, were set and are reported in Methods. The most stringent limit on the point-source origin is 1.2×10^{-9} GeV^{-1} cm^{-2} s^{-1}. Although these searches are also sensitive to very-high-energy events, the signal for an E^{-2} spectrum is expected in the TeV–PeV range and the reported limits are therefore applicable in this area.

Cosmic neutrino flux

To associate a flux to the event, the exposure of the detector for very-high-quality and high-energy tracks is computed through simulations. The exposure corresponds to selection criteria that require a good track-reconstruction likelihood (log-likelihood ratio larger than 500), a long track length within the detector (larger than 250 m) and $\mathcal{N}^{\mathrm{PMT}}_{\mathrm{trig}} > 1{,}500$.

Considering the central (90%) 72 PeV–2.6 EeV energy range, the steady isotropic flux that would produce one event is

$$E^2\Phi(E) = 5.8^{+10.1}_{-3.7} \times 10^{-8}\ \mathrm{GeV\ cm^{-2}\ s^{-1}\ sr^{-1}},$$

for which the confidence intervals are computed according to ref. 26. The 95% and 99.7% confidence level intervals are [0.30–29.8] and [0.02–47.7] $\times 10^{-8}$ GeV cm^{-2} s^{-1} sr^{-1}, respectively. This represents the KM3NeT standalone flux measurement in the 335 days of livetime of ARCA with 19 and 21 detection lines.

In Fig. 5, the flux measurement is compared with measured and predicted neutrino fluxes and limits. The KM3NeT standalone flux measurement exceeds present limits from IceCube[27] and Auger[28]. A possible interpretation is that the KM3NeT event is an upward fluctuation. In such a scenario, described in Methods, one event such as KM3-230213A would be expected in 70 years of observation with this detector configuration, and the event is an upward fluctuation at the level of 2.2σ.

The expected event rates in ARCA for various extrapolations of the flux measured by IceCube are discussed in the Supplementary Material. Considering extrapolations of the power-law fit of the IceCube measurements, these would yield at most 0.12 events in the 335 days of analysed KM3NeT data with 19 and 21 detection lines after the selection for track events described above. The observation of KM3-230213A, marginally consistent with such expectation, may hint at the emergence of a new component in the flux.

A viable alternative hypothesis is cosmogenic neutrino production[8,29,30], in which neutrinos are generated by the interaction of cosmic rays with extragalactic background light or the cosmic microwave background. The expected number of cosmogenic events in the selected data varies between 1.5×10^{-3} (ref. 31) and 0.47 (ref. 32), depending on the assumed injection spectrum and cosmic-ray mass composition, as well as the cosmological evolution of sources[31–40]. The envelope of a selection of cosmogenic models is shown as a grey-shaded band in Fig. 5. Other scenarios of diffuse emission from neutrino production in the source environment are shown as the yellow-shaded band in Fig. 5. Among these are transient emitters such as gamma-ray-bursts and tidal-disruption events[34,39,41–44], low-luminosity BL Lacs[45] and flat-spectrum radio quasars[46].

Overall, the detection of a muon neutrino with an energy greater than 100 PeV provides evidence for the existence of ultra-high-energy neutrinos in nature. The new multiPMT optical module design and the excellent optical properties of Mediterranean seawater have allowed the characterization of the neutrino interaction and have facilitated this breakthrough in neutrino astronomy.

Online content

Any methods, additional references, Nature Portfolio reporting summaries, source data, extended data, supplementary information, acknowledgements, peer review information; details of author contributions and competing interests; and statements of data and code availability are available at https://doi.org/10.1038/s41586-024-08543-1.

1. Halzen, F. & Hooper, D. High-energy neutrino astronomy: the cosmic ray connection. *Rep. Prog. Phys.* **65**, 1025 (2002).
2. Gaisser, T. K. & Stanev, T. Neutrinos and cosmic rays. *Astropart. Phys.* **39–40**, 120–128 (2012).
3. Chiarusi, T. & Spurio, M. High-energy astrophysics with neutrino telescopes. *Eur. Phys. J. C* **65**, 649–701 (2010).
4. Adrián-Martínez, S. et al. (KM3NeT Collaboration), Letter of intent for KM3NeT 2.0. *J. Phys. G: Nucl. Part. Phys.* **43**, 084001 (2016).
5. Abbasi, R. et al. (IceCube Collaboration), Improved characterization of the astrophysical muon–neutrino flux with 9.5 years of IceCube data. *Astrophys. J.* **928**, 50 (2022).
6. Abbasi, R. et al. (IceCube Collaboration), Characterization of the astrophysical diffuse neutrino flux using starting track events in IceCube. *Phys. Rev. D* **110**, 022001 (2024).
7. Abbasi, R. et al. (IceCube Collaboration), IceCube high-energy starting event sample: description and flux characterization with 7.5 years of data. *Phys. Rev. D* **104**, 022002 (2021).
8. Berezinsky, V. S. & Zatsepin, G. T. in *Proc. 11th International Conference on Cosmic Rays* 55 (Akadémiai Kiadó, 1969).
9. Aiello, S. et al. (KM3NeT Collaboration), The KM3NeT multi-PMT optical module. *J. Instrum.* **17**, P07038 (2022).
10. Aartsen, M. G. et al. (IceCube Collaboration), Evidence for high-energy extraterrestrial neutrinos at the IceCube detector. *Science* **342**, 1242856 (2013).
11. Aartsen, M. G. et al. (IceCube Collaboration), Detection of a particle shower at the Glashow resonance with IceCube. *Nature* **591**, 220–224 (2021).
12. Neyman, J. Outline of a theory of statistical estimation based on the classical theory of probability. *Philos. Trans. R. Soc. Lond. A Math. Phys. Sci.* **236**, 333–380 (1937).
13. Wilks, S. S. The large-sample distribution of the likelihood ratio for testing composite hypotheses. *Ann. Math. Stat.* **9**, 60–62 (1938).
14. Riccobene, G. et al. (NEMO Collaboration), Deep seawater inherent optical properties in the Southern Ionian Sea. *Astropart. Phys.* **27**, 1–9 (2007).
15. Albert, A. et al. (ANTARES Collaboration), Long-term monitoring of the ANTARES optical module efficiencies using ^{40}K decays in sea water. *Eur. Phys. J. C* **78**, 669 (2018).
16. Carminati, G. et al. Atmospheric MUons from PArametric formulas: a fast GEnerator for neutrino telescopes (MUPAGE). *Comput. Phys. Commun.* **179**, 915–923 (2008).
17. Ballet, J. et al. (Fermi-LAT Collaboration), Fermi Large Area Telescope Fourth Source Catalog Data Release 4 (4FGL-DR4). Preprint at https://arxiv.org/abs/2307.12546 (2023).
18. Wakely, S. P. & Horan, D. in *Proc. 30th International Cosmic Ray Conference* 1341–1344 (Universidad Nacional Autónoma de México, 2008).
19. Albert, A. et al. (HAWC Collaboration), 3HWC: the third HAWC catalog of very-high-energy gamma-ray sources. *Astrophys. J.* **905**, 76 (2020).
20. Ducoin, J.-G. et al. Optimizing gravitational waves follow-up using galaxies stellar mass. *Mon. Not. R. Astron. Soc.* **492**, 4768–4779 (2020).
21. Möller, A. et al. FINK, a new generation of broker for the LSST community. *Mon. Not. R. Astron. Soc.* **501**, 3272–3288 (2021).
22. Merloni, A. et al. The SRG/eROSITA all-sky survey. First X-ray catalogues and data release of the western Galactic hemisphere. *Astron. Astrophys.* **682**, A34 (2024).
23. Cutri, R. M. et al. VizieR Online Data Catalog: AllWISE Data Release. https://vizier.cds.unistra.fr/viz-bin/VizieR?-source=II/328 (2021).
24. Condon, J. J. et al. The NRAO VLA sky survey. *Astron. J.* **115**, 1693–1716 (1998).
25. Massaro, E. et al. The 5th edition of the Roma-BZCAT. A short presentation. *Astrophys. Space Sci.* **357**, 75 (2015).
26. Feldman, G. J. & Cousins, R. D. A unified approach to the classical statistical analysis of small signals. *Phys. Rev. D* **57**, 3873–3889 (1998).
27. Aartsen, M. G. et al. (IceCube Collaboration), Differential limit on the extremely-high-energy cosmic neutrino flux in the presence of astrophysical background from nine years of IceCube data. *Phys. Rev. D* **98**, 062003 (2018).
28. Abdul Halim, A. et al. (on behalf of the Pierre Auger Collaboration) in *Proc. 38th International Cosmic Ray Conference* 1488 (SISSA, 2023).
29. Greisen, K. End to the cosmic-ray spectrum? *Phys. Rev. Lett.* **16**, 748–750 (1966).
30. Zatsepin, G. T. & Kuz'min, V. A. Upper limit of the spectrum of cosmic rays. *J. Exp. Theor. Phys. Lett.* **4**, 78–80 (1966).
31. Berat, C. et al. Floor of cosmogenic neutrino fluxes above 10^{17} eV. *Astrophys. J.* **966**, 186 (2024).
32. Aloisio, R., Berezinsky, V. & Blasi, P. Ultra high energy cosmic rays: implications of Auger data for source spectra and chemical composition. *J. Cosmol. Astropart. Phys.* **10**, 020 (2014).
33. Muzio, M. S., Unger, M. & Wissel, S. Prospects for joint cosmic ray and neutrino constraints on the evolution of trans-Greisen-Zatsepin-Kuzmin proton sources. *Phys. Rev. D* **107**, 103030 (2023).
34. Boncioli, D., Biehl, D. & Winter, W. On the common origin of cosmic rays across the ankle and diffuse neutrinos at the highest energies from low-luminosity Gamma-Ray Bursts. *Astrophys. J.* **872**, 110 (2019).
35. Condorelli, A. et al. Testing hadronic and photohadronic interactions as responsible for ultrahigh energy cosmic rays and neutrino fluxes from starburst galaxies. *Phys. Rev. D* **107**, 083009 (2023).
36. Ehlert, D. et al. Constraints on the proton fraction of cosmic rays at the highest energies and the consequences for cosmogenic neutrinos and photons. *J. Cosmol. Astropart. Phys.* **02**, 022 (2024).
37. Muzio, M. S. & Farrar, G. R. Constraints on the hosts of UHECR accelerators. *Astrophys. J. Lett.* **942**, L39 (2023).
38. Abdul Halim, A. et al. (Pierre Auger Collaboration), Constraining the sources of ultra-high-energy cosmic rays across and above the ankle with the spectrum and composition data measured at the Pierre Auger Observatory. *J. Cosmol. Astropart. Phys.* **05**, 024 (2023).
39. Winter, W. & Lunardini, C. Interpretation of the observed neutrino emission from three tidal disruption events. *Astrophys. J.* **948**, 42 (2023).
40. Zhang, B. T. & Murase, K. Ultrahigh-energy cosmic-ray nuclei and neutrinos from engine-driven supernovae. *Phys. Rev. D* **100**, 103004 (2019).
41. Tamborra, I. & Ando, S. Diffuse emission of high-energy neutrinos from gamma-ray burst fireballs. *J. Cosmol. Astropart. Phys.* **09**, 036 (2015).
42. Yoshida, S. & Murase, K. Constraining photohadronic scenarios for the unified origin of IceCube neutrinos and ultrahigh-energy cosmic rays. *Phys. Rev. D* **102**, 083023 (2020).
43. Fang, K. et al. Testing the newborn pulsar origin of ultrahigh energy cosmic rays with EeV neutrinos. *Phys. Rev. D* **90**, 103005 (2014).
44. Heinze, J. et al. Systematic parameter space study for the UHECR origin from GRBs in models with multiple internal shocks. *Mon. Not. R. Astron. Soc.* **498**, 5990–6004 (2020).
45. Rodrigues, X. et al. Active galactic nuclei jets as the origin of ultrahigh-energy cosmic rays and perspectives for the detection of astrophysical source neutrinos at EeV energies. *Phys. Rev. Lett.* **126**, 191101 (2021).
46. Rodrigues, X. et al. Leptohadronic multi-messenger modeling of 324 gamma-ray blazars. *Astron. Astrophys.* **681**, A119 (2024).
47. Albert, A. et al. (ANTARES Collaboration), Constraints on the energy spectrum of the diffuse cosmic neutrino flux from the ANTARES neutrino telescope. *J. Cosmol. Astropart. Phys.* **08**, 038 (2024).

The KM3NeT Collaboration

S. Aiello[1], A. Albert[2,3], A. R. Alhebsi[4], M. Alshamsi[5], S. Alves Garre[6], A. Ambrosone[7,8], F. Ameli[9], M. Andre[10], M. Anghinolfi[11], L. Aphecetche[12], M. Ardid[13], S. Ardid[13], C. Argüelles[14,15], H. Atmani[16], J. Aublin[17], F. Badaracco[11,18], L. Bailly-Salins[19], Z. Bardačová[20,21], B. Baret[17], A. Bariego-Quintana[6], Y. Becherini[17], M. Bendahman[7], F. Benfenati Gualandi[22,23], M. Benhassi[7,24], M. Bennani[19], D. M. Benoit[25], E. Berbee[26], V. Bertin[5], S. Biagi[27], M. Boettcher[28], D. Bonanno[27], A. B. Bouasla[29], J. Boumaaza[16], M. Bouta[30], M. Bouwhuis[26], C. Bozza[7,31], R. M. Bozza[7,8], H. Brânzaş[32], F. Bretaudeau[12], M. Breuhaus[5], R. Bruijn[26,33], J. Brunner[5], R. Bruno[1], E. Buis[26,34], R. Buompane[7,24], S. Buson[35,36], J. Busto[5], B. Caiffi[11], D. Calvo[6], A. Capone[9,37], F. Carenini[22,23], V. Carretero[26,33], T. Cartraud[17], P. Castaldi[22,38], V. Cecchini[6], S. Celli[9,37], L. Cerisy[5], M. Chabab[39], A. Chen[40], S. Cherubini[27,41], T. Chiarusi[22], M. Circella[42], R. Cocimano[27], J. A. B. Coelho[17], A. Coleiro[17], S. Colonges[17], A. Condorelli[7,8], R. Coniglione[27], P. Coyle[5], A. Creusot[17], G. Cuttone[27], A. D'Amico[26], R. Dallier[12], A. De Benedittis[7], B. De Martino[5], G. De Wasseige[43], V. Decoene[12], I. Del Rosso[22,23], L. S. Di Mauro[27], I. Di Palma[9,37], A. F. Diaz[44], D. Diego-Tortosa[27], C. Distefano[27], A. Domi[45], C. Donzaud[17], D. Dornic[5], E. Drakopoulou[46], D. Drouhin[2,3], J.-G. Ducoin[5], R. Dvornický[21], T. Eberl[45], E. Eckerová[20,21], A. Eddymaoui[16], T. van Eeden[26], M. Eff[17], D. van Eijk[26], I. El Bojaddaini[30], S. El Hedri[17], V. Ellajosyula[11,18], A. Enzenhöfer[5], G. Ferrara[1,27], M. D. Filipović[47], F. Filippini[23], D. Franciotti[27], L. A. Fusco[7,31], S. Gagliardini[9,37], T. Gal[45], J. García Méndez[13], A. Garcia Soto[6], C. Gatius Oliver[26], N. Geißelbrecht[45], E. Genton[43], H. Ghaddari[30], L. Gialanella[7,24], B. K. Gibson[25], E. Giorgio[27], I. Goos[17], P. Goswami[17], S. R. Gozzini[6], R. Gracia[45], K. Graf[45], C. Guidi[11,18], B. Guillon[19], M. Gutiérrez[48], C. Haack[45], H. van Haren[49], A. Heijboer[26], L. Hennig[45], S. Henry[5], J. J. Hernández-Rey[6], W. Idrissi Ibnsalih[7], A. Ilioni[17], G. Illuminati[23], D. Joly[5], M. de Jong[26,50], P. de Jong[26,33], B. J. Jung[26], P. Kalaczyński[51,52], O. Kalekin[45], N. Kamp[14,15], U. F. Katz[45], G. Kistauri[53,54], C. Kopper[45], A. Kouchner[17,55], Y. Y. Kovalev[56], V. Kueviakoe[26], V. Kulikovskiy[11], R. Kvatadze[54], M. Labalme[19], R. Lahmann[45], M. Lamoureux[43], S. Lancelin[5], G. Larosa[27], C. Lastoria[19], J. Lazar[43], A. Lazo[6], S. Le Stum[5], G. Lehaut[19], V. Lemaitre[43], E. Leonora[1], N. Lessing[6], G. Levi[22,23], M. Lincetto[36], M. Lindsey Clark[17], F. Longhitano[1], N. Lumb[5], F. Magnani[5], J. Majumdar[26], L. Malerba[11,18], F. Mamedov[20], A. Manfreda[7], M. Marconi[11,18], A. Margiotta[22,23], A. Marinelli[7,8], C. Markou[46], L. Martin[12], F. Marzaioli[7,24], M. Mastrodicasa[9,37], S. Mastroianni[7], J. Mauro[43], G. Miele[7,8], P. Migliozzi[7], E. Migneco[27], M. L. Mitsou[7,24], C. M. Mollo[7], M. Mongelli[42], L. Morales-Gallegos[7,24], A. Moussa[30], I. Mozun Mateo[19], R. Muller[22], M. R. Musone[7,24], M. Musumeci[27], S. Navas[48], A. Nayerhoda[42], C. A. Nicolau[9],

B. Nkosi[40], B. Ó Fearraigh[11], V. Oliviero[7,8], A. Orlando[27], E. Oukacha[17], D. Paesani[27], J. Palacios González[6], G. Papalashvili[42,53], C. Paries[5], V. Parisi[11,18], E. J. Pastor Gomez[6], C. Pastore[42], A. M. Păun[32], G. E. Păvălaş[32], S. Peña Martínez[17], M. Perrin-Terrin[5], V. Pestel[19], R. Pestes[17], L. Pfeiffer[36], P. Piattelli[27], A. Plavin[56,57], C. Poirè[7,31], V. Popa[32,62], T. Pradier[2], J. Prado[6], S. Pulvirenti[27], C. A. Quiroz-Rangel[13], N. Randazzo[1], S. Razzaque[58], I. C. Rea[7], D. Real[6], G. Riccobene[27], J. Robinson[28], A. Romanov[11,18,19], E. Ros[56], A. Šaina[6], F. Salesa Greus[6], D. F. E. Samtleben[26,50], A. Sánchez Losa[6], S. Sanfilippo[27], M. Sanguineti[11,18], D. Santonocito[27], P. Sapienza[27], J. Schmelling[26], J. Schnabel[45], J. Schumann[45], H. M. Schutte[28], J. Seneca[26], N. Sennan[30], P. Sevle[43], I. Sgura[42], R. Shanidze[53], A. Sharma[17], Y. Shitov[20], F. Šimkovic[21], A. Simonelli[7], A. Sinopoulou[1], B. Spisso[7], M. Spurio[23,24], D. Stavropoulos[46], I. Štekl[20], M. Taiuti[11,18], Y. Tayalati[16,59], H. Thiersen[28], S. Thoudam[4], I. Tosta e Melo[1,41], B. Trocmé[17], V. Tsourapis[46], A. Tudorache[9,37], E. Tzamariudaki[46], A. Ukleja[60], A. Vacheret[19], V. Valsecchi[27], V. Van Elewyck[17,55], G. Vannoye[5], G. Vasileiadis[61], F. Vazquez de Sola[26], C. Verilhac[17], A. Veutro[9,37], S. Viola[27], D. Vivolo[7,24], A. van Vliet[4], A. Y. Wen[14,15], E. de Wolf[26,33], I. Lhenry-Yvon[17], S. Zavatarelli[11], A. Zegarelli[9,37], D. Zito[27], J. D. Zornoza[6], J. Zúñiga[6] & N. Zywucka[28]

[1]INFN, Sezione di Catania (INFN-CT), Catania, Italy. [2]Université de Strasbourg, CNRS, IPHC UMR 7178, Strasbourg, France. [3]Université de Haute Alsace, Mulhouse, France. [4]Department of Physics, Khalifa University, Abu Dhabi, United Arab Emirates. [5]Aix Marseille Université, CNRS/IN2P3, CPPM, Marseille, France. [6]IFIC - Instituto de Física Corpuscular (CSIC - Universitat de València), Paterna, Spain. [7]INFN, Sezione di Napoli, Complesso Universitario di Monte S. Angelo, Napoli, Italy. [8]Università di Napoli "Federico II", Dip. Scienze Fisiche "E. Pancini", Complesso Universitario di Monte S. Angelo, Napoli, Italy. [9]INFN, Sezione di Roma, Roma, Italy. [10]Laboratori d'Aplicacions Bioacústiques, Centre Tecnològic de Vilanova i la Geltrú, Universitat Politècnica de Catalunya, Vilanova i la Geltrú, Spain. [11]INFN, Sezione di Genova, Genova, Italy. [12]Subatech, IMT Atlantique, IN2P3-CNRS, Nantes Université, Nantes, France. [13]Instituto de Investigación para la Gestión Integrada de las Zonas Costeras, Universitat Politècnica de València, Gandia, Spain. [14]Department of Physics, Harvard University, Cambridge, MA, USA. [15]Laboratory for Particle Physics and Cosmology, Lyman Laboratory, Harvard University, Cambridge, MA, USA. [16]Faculty of Sciences, University Mohammed V in Rabat, Rabat, Morocco. [17]Astroparticule et Cosmologie, Université Paris Cité, CNRS, Paris, France. [18]Università di Genova, Genova, Italy. [19]LPC CAEN, Normandie Université, ENSICAEN, UNICAEN, CNRS/IN2P3, Caen, France. [20]Institute of Experimental and Applied Physics, Czech Technical University in Prague, Prague, Czech Republic. [21]Department of Nuclear Physics and Biophysics, Comenius University, Bratislava, Slovak Republic. [22]INFN, Sezione di Bologna, Bologna, Italy. [23]Dipartimento di Fisica e Astronomia, Università di Bologna, Bologna, Italy. [24]Dipartimento di Matematica e Fisica, Università degli Studi della Campania "Luigi Vanvitelli", Caserta, Italy. [25]E. A. Milne Centre for Astrophysics, University of Hull, Hull, United Kingdom. [26]Nikhef, National Institute for Subatomic Physics, Amsterdam, The Netherlands. [27]INFN, Laboratori Nazionali del Sud (LNS), Catania, Italy. [28]Centre for Space Research, North-West University, Potchefstroom, South Africa. [29]Département de Physique, Faculté des Sciences, Laboratoire de Physique des Rayonnements, Université Badji Mokhtar-Annaba, Annaba, Algeria. [30]Faculty of Sciences, University Mohammed I, Oujda, Morocco. [31]Dipartimento di Fisica, Università di Salerno e INFN Gruppo Collegato di Salerno, Fisciano, Italy. [32]Institute of Space Science (ISS), Măgurele, Romania. [33]Institute of Physics/IHEF, University of Amsterdam, Amsterdam, The Netherlands. [34]Technical Sciences, TNO, Delft, The Netherlands. [35]Deutsches Elektronen-Synchrotron (DESY), Zeuthen, Germany. [36]Fakultät für Physik und Astronomie, Institut für Theoretische Physik und Astrophysik, Lehrstuhl für Astronomie, Julius-Maximilians-Universität Würzburg, Würzburg, Germany. [37]Dipartimento di Fisica, Università La Sapienza, Roma, Italy. [38]Dipartimento di Ingegneria dell'Energia Elettrica e dell'Informazione "Guglielmo Marconi", Università di Bologna, Cesena, Italy. [39]Physics Department, Faculty of Science Semlalia, Cadi Ayyad University, Marrakech, Morocco. [40]School of Physics, University of the Witwatersrand, Johannesburg, South Africa. [41]Dipartimento di Fisica e Astronomia "Ettore Majorana", Università di Catania (INFN-CT), Catania, Italy. [42]INFN, Sezione di Bari, Bari, Italy. [43]Centre for Cosmology, Particle Physics and Phenomenology, UCLouvain, Louvain-la-Neuve, Belgium. [44]Department of Computer Engineering, Automation, and Robotics, CITIC, University of Granada, Granada, Spain. [45]Erlangen Centre for Astroparticle Physics, Friedrich-Alexander-Universität Erlangen-Nürnberg (FAU), Erlangen, Germany. [46]Institute of Nuclear and Particle Physics, NCSR Demokritos, Athens, Greece. [47]School of Computing, Engineering and Mathematics, Western Sydney University, Penrith, New South Wales, Australia. [48]Departamento de Física Teórica y del Cosmos and CAFPE, University of Granada, Granada, Spain. [49]Royal Netherlands Institute for Sea Research (NIOZ Texel), Den Burg, The Netherlands. [50]Leiden Institute of Physics, Leiden University, Leiden, The Netherlands. [51]AstroCeNT, Nicolaus Copernicus Astronomical Center, Polish Academy of Sciences, Warsaw, Poland. [52]Center of Excellence in Artificial Intelligence, AGH University of Krakow, Krakow, Poland. [53]Department of Physics, Tbilisi State University, Tbilisi, Georgia. [54]Institute of Physics, University of Georgia, Tbilisi, Georgia. [55]Institut Universitaire de France, Paris, France. [56]Max-Planck-Institut für Radioastronomie, Bonn, Germany. [57]Black Hole Initiative, Harvard University, Cambridge, MA, USA. [58]Department Physics, University of Johannesburg, Auckland Park, South Africa. [59]Institute of Applied Physics, Mohammed VI Polytechnic University, Ben Guerir, Morocco. [60]National Centre for Nuclear Research, Warsaw, Poland. [61]Laboratoire Univers et Particules de Montpellier, Montpellier, France. [62]Deceased: V. Popa.

Methods

The detector

The KM3NeT detectors[4] are three-dimensional arrays of photosensors installed at great depths in the Mediterranean Sea. The sensors detect the Cherenkov radiation induced in seawater by relativistic charged particles. They are housed in optical modules[9], which are 44-cm-diameter pressure-resistant glass spheres, each with 31 3-inch PMTs. Each optical module contains data-acquisition electronics and calibration instrumentation. The modules of the ARCA detector, located at a depth of 3,450 m offshore Portopalo di Capo Passero, Sicily, in the Mediterranean Sea, are chained together in groups of 18, spaced by 36 m, along 700-m-long vertical detection lines anchored to the seabed and kept taut by the buoyancy of the optical modules and top buoys. An electro-optical cable runs along the detection lines, powering the optical modules and transporting data through optical fibres. Detection lines are placed on the seafloor with an average horizontal spacing of 95 m. At the time of the event, the ARCA detector consisted of 21 detection lines. The instrumented volume, that is, the smallest cylinder containing all optical modules, was about 0.15 km^3. In its final configuration, the array will comprise 230 detection lines.

The data-acquisition system is based on the 'all-data-to-shore' concept: all analogue signals from the PMTs above a certain tunable threshold are digitized offshore and all digital data are sent to shore, where they are processed in real time. The data contain the time stamp of the leading edge and the pulse length of the time-over-threshold signal from a discriminator, jointly referred to as 'hit'. The time-over-threshold is proportional to the number of converted photoelectrons on the PMT. Although the linear behaviour holds relatively well for pulses up to a few tens of photoelectrons, above 30 photoelectrons, a saturation effect is observed, producing a flattening of the time-over-threshold measurements with increasing charge[9].

Trigger algorithms search for clusters of hits correlated in space and time. Local coincidences of hits are identified on each optical module within a 25-ns time window. Then, three different clustering algorithms are applied, assuming that hits come from light propagating according to a possible track or shower origin. A space-time coincidence between at least five hits on five modules within 250 m, under the assumption that light expands from a point-like source, constitute a cluster for the nominal shower trigger, allowing for a 25-ns delay to light propagation in water. A similar condition is applied for the track trigger, but this time considering that the light source is a track that moves in the detector at the speed of light in vacuum, and searching for hits in a cylinder of radius 120 m. A low-threshold shower trigger is also applied, requiring coincidences of eight hits on three modules within 110 m. When one or more clusters are found, all data from an $\mathcal{O}(10)$-μs time window are recorded as an event for offline calibration and processing. Triggering criteria are designed to detect events at the lower-energy threshold. In the case of KM3-230213A, 3,659 individual (overlapping) trigger clusters were found in the time window and $\hat{N}_{\mathrm{trig}}^{\mathrm{PMT}} = 3{,}672$ PMTs participated to form at least one of those trigger clusters. PMTs that have recorded hits but that do not participate in any trigger cluster are predominantly caused by optical backgrounds that are very far away and/or not time-correlated with the physical event. It is for this reason that $\hat{N}_{\mathrm{trig}}^{\mathrm{PMT}}$ is used as observable for the energy estimate.

Data-quality criteria are applied to reject periods with detector instabilities from the analysis sample.

Detector simulation

High-energy neutrino events (100 GeV < E_ν < 100 EeV) were simulated with gSeaGen v7.4.3 (refs. 48,49), using GENIE[50] to simulate the neutrino interaction by means of the HEDIS package[51,52]. The deep-inelastic scattering model CSMS11 (ref. 53) was used. PROPOSAL[54] and TAUSIC[55] were used by gSeaGen to propagate muons and taus up to the detector.

The accurate simulation of the light produced by a muon of a given energy is crucial to the muon energy estimate. KM3NeT uses proprietary code, which simulates the continuous and stochastic energy losses owing to bremsstrahlung, pair production, photonuclear interactions, delta rays and ionization, as well as the multiple Coulomb scattering and deep-inelastic scattering. Differential cross-sections for the main processes are extracted from refs. 56,57. The light produced by the muon and the secondary particles is simulated by sampling photon tables that contain the probability density functions of the arrival time of Cherenkov light on a PMT as a function of the distance from the emission point and the PMT orientation with respect to the particle[58]. For secondary particles, equivalent tabulated values for electromagnetic shower light are used. The amount of photons generated depends on the type and energy of the particle and has been adjusted according to Geant4 simulations[59].

The photon tables account for light absorption, scattering and chromatic dispersion. Absorption is modelled on the basis of in situ measurements[14]; the scattering model for seawater accounts for pure-water scattering, following the Einstein and Smoluchowski description[60,61], and particle scattering, accounting for the wavelength dependence using the Kopelevich parameterization[62] and considering the Petzold data[63] for the angular dependence. The angular acceptance and average quantum efficiency of the PMTs are also accounted for in the tables, as derived from detailed simulations of the PMT and the structure of the optical module[64], and from laboratory measurements[65].

The simulation of the stochastic energy losses has been cross-checked by comparing the total simulated amount of energy lost by the muon over a given distance with the same quantity computed using the PROPOSAL software[54]. Agreement at better than the 10% level was found over the whole energy range of interest. Moreover, PROPOSAL has also been used to check that varying the theoretical models used to describe energy losses[66–69] yields differences that are within the stochastic fluctuations of the energy-loss processes.

Because no external data are available in this energy range to validate the simulation procedure, the particle-propagation and light-simulation code has also been compared with state-of-the-art Geant4-based[59] simulation and with a custom GPU-based photon-tracking code (https://github.com/PLEnuM-group/PhotonPropagation.jl) in which the same water model and detector response have been implemented in an independent way. The output of these simulations are in good agreement; when using the alternative simulations for the energy measurement, the result is within 10% of the nominal value.

After light simulation, the readout is simulated. The conversion from photoelectrons on the cathode of the PMT to a time-over-threshold measurement and the transit-time distributions of the PMTs reproduce laboratory measurements[65]. The gain, gain spread and relative PMT efficiencies come from in situ measurements[70]. Afterpulses in the PMTs are at present not simulated. Optical background rates and the status of each PMT in the detector are simulated using the rates measured in the detector, following the run-by-run approach pioneered by the ANTARES Collaboration[71,72]. Subsequently, the simulated data are subjected to the same trigger and reconstruction algorithms that are applied to the data. Comparisons between data and Monte Carlo simulations are provided in Extended Data Fig. 1 for a loose event selection in which the sample is dominated by atmospheric muons. Wrongly reconstructed atmospheric muons that appear as upgoing events in the zenith distribution are completely removed once the selection on the reconstruction log-likelihood is applied.

Event reconstruction

The directional reconstruction of the muon track is performed with the standard algorithm, which is based on the arrival time of the Cherenkov photons at the PMTs[73]. Under the hypothesis that a muon travelling in direction $\vec{d}$ is at position $\vec{p}_0$ at time t_0, the arrival time of the Cherenkov light at position $\vec{q}$ is

$$t = t_0 + z/c + \frac{D}{\sin(\theta_C)} v_g^{-1}, \quad (1)$$

in which D is the distance of closest approach of the muon to $\vec{q}$ and z is the distance the muon travels before emitting a photon under angle θ_C, $z = \vec{d} \cdot (\vec{q} - \vec{p}_0) - \frac{D}{\tan\theta_C}$; v_g is the group velocity of light at a reference wavelength of 460 nm.

The reconstruction algorithm maximizes the likelihood of the arrival time residuals

$$\mathcal{L} = \prod_i p(r_i, d_i, \phi_i, \theta_i), \quad (2)$$

in which p denotes the probability density function of the arrival time residual r_i, obtained from interpolated photon tables, at a distance d_i from the emission point. The angles ϕ_i and θ_i describe the orientation of the PMT with respect to the track direction. The photon tables are the same as those that have been described above for the simulation of light from the muon trajectory. They include the contribution of optical background.

The algorithm uses only the first hit on each PMT, as they carry most of the information on the muon direction. As a result of this choice, the reconstruction is robust against PMT afterpulses and other details of modelling of later hits. For the likelihood maximization, only the first hits in a cylinder of radius 175 m and axis defined by the prefit direction are used. This is the standard setting, which was chosen as it optimizes the speed of the algorithm. In the case of KM3-230213A, there are hits outside this cylinder, but it was tested that including them alters the reconstructed track by less than the statistical uncertainty on the direction.

To mitigate the effect of local minima on the likelihood function, the maximization is preceded by a prefit, scanning in 4π sr over assumed track directions. This procedure generates a set of starting points for the likelihood maximization. The track with the largest likelihood is retained.

For ascertaining the quality of the events, the log-likelihood ratio, $\log(\mathcal{L}/\mathcal{L}_b)$ is used, with $\mathcal{L}_b$ the likelihood computed for the case of only optical background hits. This quantity effectively quantifies the number of hits whose arrival time matches the expectation from the track hypothesis. Typical well-reconstructed muons have a value ≳50, with a tail of larger values resulting from well-reconstructed events with many hits. KM3-230213A has a log-likelihood ratio of 1,415.2, which is the highest value observed in the 21-line ARCA data.

To illustrate the quality of the reconstruction, Extended Data Fig. 2 presents the photon arrival time residuals, which represent the difference between the measured time and the expected time from the reconstructed muon trajectory hypothesis, shown here for the first hits on the PMTs. Many hits are compatible with the muon hypothesis with nanosecond accuracy, even for PMTs located far from the track. Hits arriving after the main peak are because of photons that have scattered in the water and/or that were emitted under some angle other than θ_C from the muon track. These contributions are accounted for in the reconstruction and the large log-likelihood ratio value reflects the agreement of these residuals with the detailed expectation.

Pointing of the telescope

The directional uncertainty on the event is dominated by uncertainty on the absolute orientation of the detector on Earth.

Compasses and accelerometers in the optical modules allow for an estimation of their orientation. The detection lines move with the sea current, which can displace the top modules by $\mathcal{O}(10)$ m. The continuous monitoring of the optical module positions is therefore mandatory. For this purpose, a system of autonomous acoustic emitters is used, located in and up to 1 km outside the detector on the seabed[74]. The acoustic signals are recorded by piezoelectric sensors in the optical modules. A χ^2 fit of the arrival times of the sound is used to determine the orientation and shape of the detection line as parameterized by a mechanical model. In this way, the relative positions of the optical modules can be determined to within 0.15 m. Acoustic signals are processed at 10-min intervals; the results of the fit are interpolated to provide the relative positions of the optical modules over time[75]. At the time of the event, the string tilts changed steadily by about 2° over a time span of 2 h, corresponding to less than 0.1° in 10 min. The uncertainty on the position of the detector elements owing to the interpolation of the acoustic data is thus negligible.

The acoustic system measures distances between the optical modules and acoustic emitters but this does not constrain the absolute orientation of the telescope on Earth. During sea campaigns, the positions of the detection lines and acoustic emitters are measured. The emitter positions are used to determine the nominal absolute orientation. These data are at a present accurate to approximately 10 m. This is supported by comparisons with two bathymetry datasets (for the vertical positions) and internal cross-checks with the acoustic system (for the horizontal positions). The position uncertainty translates, after conservatively rounding the result, to an uncertainty of 1° on rotations of the detector around each of the three axes.

An independent cross-check of the pointing was performed by means of a measurement of the directional deficit of atmospheric muons owing to the absorption of cosmic rays in the Moon, similar to ref. 76. This anti-signal of the Moon was studied in 335 days of data when the detector consisted of 19 and 21 detection lines. The Moon shadow signal was found at a significance of 3.2σ. In evaluating the Moon shadow for different assumed rotations around the vertical axis, in the range ±3° in steps of 0.25°, the largest significance was found for the nominal orientation. The corresponding uncertainty is evaluated by means of simulations to 0.24°.

A comparison of detector-line depths determined with the acoustic system and the two bathymetry datasets yields further evidence that the system is aligned to within 1°.

Propagating the 1° uncertainty to the celestial coordinates of the event yields a circular 68% confidence region on the sky with a radius of 1.5°. This uncertainty is the dominant source of (systematic) uncertainty in the determination of the celestial coordinates of KM3-230213A.

Simulations of muons in the same location as KM3-230213A were performed at energies from 1 to 1,000 PeV to evaluate the statistical uncertainty on the direction estimation. At 100 PeV, 50% (90%) of the muons are reconstructed within 0.12° (0.28°) from the nominal direction. The azimuthal uncertainty increases with energy, so that, for an energy of 500 PeV, 50% (90%) of the muons were reconstructed within 0.17° (0.38°). These uncertainties are negligible with respect to the 1.5° 68% confidence region and are mentioned here only to indicate the future potential of a fully aligned detector.

We foresee upgrading the detector in the next sea campaign by using new acoustic emitters whose absolute position will be measured with <1-m accuracy in each direction. This, as well as the extra collected data for the Moon shadow analysis, will allow for a recalibration of the data and a more precise determination of the celestial origin of KM3-230213A.

Energy estimate

The energy of a muon above a few TeV can be estimated by measuring its energy loss. Radiative energy losses produce showers of charged particles along the muon trajectory that induce excess Cherenkov photons along the track. The photons arrive on the PMTs very close in time, producing a large number of photoelectrons that translate into hits with a large time-over-threshold. In the case of KM3-230213A, the large number of photons induced by the muon saturates most of the PMTs within about 100 m from the track, and hits are recorded even up to a distance of 300 m. This saturation effect is visible in more than 25% of the PMTs that participated in the triggering of KM3-230213A

and is reproduced in simulations. Several subsequent hits are observed on the PMTs and at least some of them could be attributed to afterpulses, which are not modelled in the Monte Carlo simulations. The number of PMTs that participate in the triggering of the event, $\mathcal{N}_{\mathrm{trig}}^{\mathrm{PMT}}$, is used as an observable in the energy estimation to overcome this possible issue. This observable does not exploit the full information from the event, as it does not account for the time-over-threshold information, but is robust against the limitations of the simulations because PMTs are only counted once if several hits are recorded.

Simulations of muons of various energies traversing the detector in the same direction and location as the reconstructed event were used to estimate the energy of KM3-230213A. The optical properties of water (scattering and absorption lengths) and the detection efficiency of the optical modules were varied in the simulation to account for systematic uncertainties, within the known limits for these parameters. The estimate of the muon energy E_{μ} is derived from the likelihood $\mathcal{L}(E_{\mu}, \vec{\xi}; \mathcal{N}_{\mathrm{trig}}^{\mathrm{PMT}})$, in which $\vec{\xi}$ are nuisance parameters that affect the $\mathcal{N}_{\mathrm{trig}}^{\mathrm{PMT}}$ distribution. The likelihood $\mathcal{L}$ is estimated from the aforementioned Monte Carlo simulations at discrete combinations of E_{μ} and the three nuisance parameters. A Gaussian term is added to the likelihood to constrain each of the nuisance parameters to within 10% (1σ) of the nominal value. The energy estimate is the value that maximizes the constrained likelihood. The maximum-likelihood values for given $\mathcal{N}_{\mathrm{trig}}^{\mathrm{PMT}}$ are shown in Extended Data Fig. 3 left, with the 68% confidence level interval with and without systematic uncertainties, computed from Wilks' theorem[13]. The log-likelihood profile for $\hat{\mathcal{N}}_{\mathrm{trig}}^{\mathrm{PMT}} = 3{,}672$ is shown in the right panel of Extended Data Fig. 3, with the 1σ, 2σ and 3σ confidence levels, with and without systematics.

Scattering of light does not influence the energy estimate by more than several percent. Similarly, it was found that the optical module efficiency has a <10% level effect on this estimation. The most relevant effect comes from light absorption: a +10% (−10%) modification of the absorption length yields a −0.21 (+0.25) shift in the logarithm of the estimated energy. Finally, it was checked that modifying the muon direction and location in the simulations, within the estimated systematic uncertainties from the detector calibration, does not affect the energy measurement.

The incoming neutrino energy is estimated using Monte Carlo simulations in which neutrino interactions are simulated over a large volume surrounding the detector. Because the neutrino interaction point is unknown, a flat prior is assumed on the muon propagation length in case the interaction occurred in the sensitive volume of the detector, up to 350 m away from the instrumented volume. If instead the interaction occurred outside the sensitive volume, the muon propagation distance distribution is taken from the large-scale Monte Carlo productions obtained with the standard KM3NeT simulation chain. Neutrino events are weighted according to a power-law spectrum with a spectral index equal to −2 to finally estimate the neutrino energy distribution that would produce muons at the detector distributed according to the energy estimate and its uncertainty.

Background evaluation

Atmospheric muons from cosmic-ray extensive air showers constitute most of the events reconstructed in neutrino telescopes. The probability that KM3-230213A is an atmospheric muon is constrained from its reconstructed direction and energy. The muon flux drops rapidly with energy; given that the primary flux of ultra-high-energy cosmic rays extends up to at most several hundred EeV (refs. 77,78), muons at sea level cannot exceed an energy of few tens of EeV, as muons carry on average around 10% of the primary energy. However, the flux of atmospheric muons at high energies is affected by several uncertainties, such as those on the flux and spectrum of primary cosmic rays, on the composition of this flux, on the hadronic interactions of cosmic rays and of their interaction products. For this reason, a conservative estimate of the surviving muon background has been obtained using a toy model in which several muons have been injected on the surface of the sea according to a power-law spectrum with spectral index −2.7 and normalization at 100 PeV equal to 10^{-17} GeV cm^{-2} s^{-1} sr^{-1}. These assumptions yield an overestimation of the muon flux by at least one order of magnitude over the whole energy range of interest, so that a conservative estimate of the rate of muons reaching the detector can be obtained.

Muons in the EeV range and beyond have a maximal range of about 60 km in water. Requiring that they must reach the detector still with at least an energy of 10 PeV reduces their effective range to about 30 km. Given the curvature of the Earth and the measured zenith angle, a muon should have entered the water at a distance of approximately 140 km from the detector. The direction of the event points towards the Malta Escarpment, a cliff rising above the abyssal plain: an atmospheric muon travelling in this direction should cross it to reach the detector. In Extended Data Fig. 4, bathymetric data have been used to show the path travelled by a particle along the reconstructed direction. Assuming an average density of 2.6 g cm^{-3} for rock in the seabed, the total amount of matter to be traversed is then on the order of 300 km water-equivalent for the reconstructed direction and becomes smaller than 60 km only if the absolute orientation of the detector is wrong by more than 2° in zenith.

Even assuming a flux that overshoots by one order of magnitude the total flux of atmospheric muons, and including the uncertainties on the zenith angle reconstruction for KM3-230213A, the upper limit on the muon rate is $\ll 10^{-10}$ events per year when assuming a direction within 2σ of the best-fit value. For a mis-reconstruction at a 5σ level error, the upper limit is still $\ll 10^{-4}$ events per year for the single-muon hypothesis and $\ll 10^{-3}$ events per year for muon bundles of low multiplicity in which only a few parallel muons from the same cosmic-ray air shower could reach the detector. This estimation is confirmed when extrapolating the expected rate of events from Monte Carlo simulations[16] accounting for muon absorption in water following ref. 79.

Bundles of downgoing (zenith angles smaller than 60°) atmospheric muons, or muons from simultaneous but unrelated cosmic-ray air showers, can produce a large amount of light in the detector. Such events could be mis-reconstructed as a horizontal track. Such coincidences would, however, not have good hit-residuals distributions on all PMTs over many detection lines, in contrast to what is observed for KM3-230213A. This is further corroborated by the detection of several showers along the muon path and their collinearity (as shown in the Supplementary Material): given the good time resolution of the detector elements, a nanosecond-level temporal coincidence between the arrival time of muons at the detector and the emission of showers along their track would be needed to create such a light pattern in the detector, which is extremely unlikely.

Considering the reconstructed arrival direction, neutrinos from cosmic-ray interactions in the atmosphere are not substantially absorbed at least up to some tens of EeV. However, the flux of these atmospheric neutrinos falls steeply with energy. The conventional component, arising from pion and kaon decays in the cosmic-ray extensive air shower, fades away at an energy of about 100 TeV–1 PeV. In that energy range, a prompt component is expected to arise from the decay of short-lived charmed hadrons and become the dominant contribution to the atmospheric flux. Reference neutrino conventional and prompt fluxes were computed using the MCEq software[80] and the Sibyll 2.3c hadronic interaction model[81], for the location of the ARCA detector: the expected event rates above 100 PeV in the detector are on the order of $(1–5) \times 10^{-5}$ events per year, depending on the chosen model of the primary cosmic-ray flux[82]. Estimations of prompt fluxes are affected by large uncertainties[83]; even considering the most optimistic estimations, the event rate from prompt atmospheric neutrinos is less 5×10^{-3} events per year. An alternative possibility could be that the detected muon does not come from the interaction of a ν_{μ} from the prompt component but rather arises from the decay of a tau lepton from the

prompt atmospheric ν_τ flux. The branching ratio of charmed hadrons to ν_τ is about a tenth of that to muon neutrinos, hence the expected flux in the atmosphere is one order of magnitude lower. However, above EeV energies, the tau decay length (>50 km) increases the effective volume for the detection of these neutrino interactions. Nonetheless, the prompt flux still remains too low to explain the observed event, with an estimated event rate from atmospheric prompt tau neutrinos $\leq 10^{-5}$ events per year for the flux estimated with the Sibyll 2.3c hadronic interaction model.

Search for point-like neutrino sources

Data of different configurations of the ARCA and ORCA detectors, as well as the public data of the ANTARES and IceCube experiments, have been analysed to evaluate a possible directional excess of neutrinos close to KM3-230213A. Details on the analysed datasets and respective analysis methods are given in Extended Data Table 1. Depending on the available frameworks, either an ON/OFF method or a maximum-likelihood approach (binned or unbinned) was used. In the latter case, the inspected region was divided into pixels covering equal areas (about 0.1° × 0.1°) in solid angle by using the HEALPix tool[84] with a value of N_{side} parameter of 512 and the likelihood was maximized in each pixel. The results are summarized in Extended Data Table 2.

Searches for counterpart candidates

Four selection methods have been applied to astronomical catalogues to build a counterpart blazar candidate sample. The searches were performed within 3° from KM3-230213A (99% event error region).

Method 1. Archival wavelength data were used to pinpoint a blazar counterpart: X-ray sources from the first eROSITA catalogue[22] were cross-matched with the radio NVSS catalogue[24], selecting 18 sources with radio flux greater than 10 mJy. Infrared data collected by WISE[23] were used to further refine the list of possible counterparts. Blazars populating the 'WISE blazar strip'[85] were selected, narrowing the list of candidate blazars to seven objects.

Method 2. Following the approach suggested in ref. 86, measurements from Very Long Baseline Interferometry (VLBI) from the Radio Fundamental Catalog (RFC 2024b (https://astrogeo.org/rfc/)) were used. All sources above its present completeness cutoff of 100 mJy at 8 GHz were selected, resulting in five objects with median VLBI flux density ranging from 0.1 to greater than 2 Jy, as in Extended Data Table 3.

Method 3. The Roma-BZCAT[25] has been used to search for active galactic nuclei correlations. This blazar catalogue contains 3,561 sources, compiling the results of multifrequency observations. Three blazars were found in this catalogue.

Method 4. The 4FGL-DR4 catalogue[17] is the latest compilation of gamma-ray sources observed by the Fermi-LAT instrument in 14 years of survey data in the 50 MeV–1 TeV energy range: four sources were selected.

The main properties of the selected sources and the respective selection method(s) are described in Extended Data Table 3.

Exposure and tension computation

The KM3NeT/ARCA all-sky exposure is defined as:

$$\mathcal{E}^{\mathrm{KM3NeT}}(E) = 4\pi \times T^{\mathrm{KM3NeT}} \times A_{\mathrm{eff}}^{\mathrm{KM3NeT}}(E) \tag{3}$$

in which $T^{\mathrm{KM3NeT}} = 335$ days (covering the 19 and 21 detection line configurations of ARCA) and $A_{\mathrm{eff}}^{\mathrm{KM3NeT}}$ is the sky-averaged effective area, shown in Extended Data Fig. 5, averaged between neutrinos and antineutrinos. This effective area has been estimated for the track selection described in the text ($\mathcal{N}_{\mathrm{trig}}^{\mathrm{PMT}} > 1{,}500$, track length longer than 250 m and track-reconstruction log-likelihood ratio larger than 500). The expected number of events for a per-flavour $\nu + \bar{\nu}$ all-sky flux Φ is then simply:

$$n_{\mathrm{expected}}^{\mathrm{KM3NeT}} = \int_{E_{\mathrm{min}}^{\mathrm{KM3\text{-}230213A}}}^{E_{\mathrm{max}}^{\mathrm{KM3\text{-}230213A}}} \mathcal{E}^{\mathrm{KM3NeT}}(E) \times \Phi(E)\mathrm{d}E, \tag{4}$$

in which the integration bounds are fixed to the central 90% neutrino energy range associated with KM3-230213A.

The all-sky exposures $\mathcal{E}^{\mathrm{Auger}}(E)$ and $\mathcal{E}^{\mathrm{IceCube}}(E)$, averaged between neutrinos and antineutrinos, have been estimated using published material. The effective area of the Pierre Auger Observatory was taken from the data release from ref. 87, for the three analysis samples (Earth-skimming, low-zenith downward-going, high-zenith downward-going), with a livetime of 18 years. The IceCube/EHE all-flavour effective area was taken from the 9-year analysis sample[88].

Assuming a per-flavour single-power-law diffuse neutrino flux $\Phi(E) = \phi(E(\mathrm{GeV}))^{-2}$, we may estimate the most probable flux normalization $\hat{\phi}$ given one observed event in KM3NeT and zero events in Auger and IceCube/EHE samples, using a maximum-likelihood estimator with Poisson likelihoods: $\hat{\phi} = 7.5 \times 10^{-10}$ GeV cm^{-2} s^{-1} sr^{-1}.

For such a flux, 0.59 and 0.40 events would be expected in IceCube and Auger, respectively, which is compatible with their null observations. The corresponding expected number of events in KM3NeT is about 0.013 events, hence hinting at a 2.2σ upward fluctuation. The joint Poisson probability of such a configuration (one event in KM3NeT and zero in IceCube and Auger) is about 0.5% (2.6σ).

Inclusion & ethics statement

The scientific objectives of the KM3NeT Collaboration are the search for and observation of sources in the Universe of high-energy cosmic neutrinos and the measurement of characteristics of neutrinos generated in the Earth's atmosphere. For this, the Collaboration is building a network of neutrino detectors at the bottom of the Mediterranean Sea. At the same locations, the network also provides nodes for the connection of instruments for Earth and sea science studies. Building the detectors with instrumented volumes of up to several cubic kilometres will take several years. Scientific analyses of the recorded data are conducted under the supervision of the Collaboration; after several years, the data will be made available to others as described in the KM3NeT data dissemination plan.

The scientists and engineers in the KM3NeT Collaboration that have come together because they share the scientific interest and come from different backgrounds, cultures and countries. This diversity is considered a strength of the Collaboration and a basis for high-quality research. To nurture the diversity, the Collaboration has developed a code of conduct and ethical behaviour built on a set of shared values and describing rules of good conduct.

The formal rules for the Collaboration are described in a Memorandum of Understanding (MoU) signed by the funding authorities of the institutes employing the individuals participating in the KM3NeT Collaboration.

Data availability

Raw experimental data from the KM3NeT detectors are not made publicly accessible, owing to the high complexity and volume of the data. Processed data and code to reproduce part of the above findings are available as a Zenodo repository (https://doi.org/10.5281/zenodo.13366058)[89] under an open license. Source data are provided with this paper.

Code availability

Sample code to analyse the available data to reproduce part of the above findings is available as a Zenodo repository at https://doi.org/10.5281/zenodo.13366058 (ref. 89) under an open license.

48. Aiello, S. et al. (KM3NeT Collaboration), gSeaGen: the KM3NeT GENIE-based code for neutrino telescopes. *Comput. Phys. Commun.* **256**, 107477 (2020).
49. Distefano, C., Garcia, A. & Kalaczyński, P. gSeaGen v7.4.3. *Zenodo* https://doi.org/10.5281/zenodo.10926624 (2024).
50. Andreopoulos, C. et al. The GENIE neutrino Monte Carlo generator. *Nucl. Instrum. Methods Phys. Res. A* **614**, 87–104 (2010).
51. Alvarez-Ruso, L. et al. Recent highlights from GENIE v3. *Eur. Phys. J. Spec. Top.* **230**, 4449–4467 (2021).
52. Garcia Soto, A. et al. Complete predictions for high-energy neutrino propagation in matter. *J. Cosmol. Astropart. Phys.* **09**, 025 (2020).
53. Cooper-Sarkar, A. et al. The high energy neutrino cross-section in the Standard Model and its uncertainty. *J. High Energy Phys.* **2011**, 42 (2011).
54. Koehne, J.-H. et al. PROPOSAL: a tool for propagation of charged leptons. *Comput. Phys. Commun.* **184**, 2070–2090 (2013).
55. Antonioli, P. et al. A three-dimensional code for muon propagation through the rock: MUSIC. *Astropart. Phys.* **7**, 357–368 (1997).
56. Zyla, P. A. et al. (Particle Data Group), Review of particle physics. *Prog. Theor. Exp. Phys.* **2020**, 083C01 (2020).
57. Abramowicz, H. et al. (ZEUS Collaboration), Measurement of the energy dependence of the total photon–proton cross section at HERA. *Phys. Lett. B* **697**, 184–193 (2011).
58. de Jong, M. & van Campenhout, E. The probability density function of the arrival time of Čerenkov light. Preprint at https://arxiv.org/abs/2305.19626 (2023).
59. Agostinelli, S. et al. Geant4—a simulation toolkit. *Nucl. Instrum. Methods Phys. Res. A* **506**, 250–303 (2003).
60. Einstein, A. Theorie der Opaleszenz von homogenen Flüssigkeiten und Flüssigkeitsgemischen in der Nähe des kritischen Zustandes. *Ann. Phys.* **338**, 1275–1298 (1910).
61. Smoluchowski, M. V. Molekular-kinetische Theorie der Opaleszenz von Gasen im kritischen Zustande, sowie einiger verwandter Erscheinungen. *Ann. Phys.* **330**, 205–226 (1908).
62. Kopelevich, O. V. in *Ocean Optics* Vol. 19 (ed. Monin, A.) Ch. 8 (Nauka, 1983).
63. Petzold, T. J., *Volume Scattering Functions for Selected Ocean Waters* (Scripps Institution of Oceanography, 1972).
64. Hugon, C. M. F. in *Proc. 34th International Cosmic Ray Conference* 1106 (SISSA, 2015).
65. Aiello, S. et al. (KM3NeT Collaboration), Characterisation of the Hamamatsu photomultipliers for the KM3NeT neutrino telescope. *J. Instrum.* **13**, P05035 (2018).
66. Abramowicz, H. & Levy, A. The ALLM parameterization of $\sigma_{tot}(\gamma^*p)$ - an update. Preprint at https://arxiv.org/abs/hep-ph/9712415 (2004).
67. Abt, I. et al. Investigation into the limits of perturbation theory at low Q^2 using HERA deep inelastic scattering data. *Phys. Rev. D* **96**, 014001 (2017).
68. Kelner, S. R., Kokoulin, R. P. & Petrukhin, A. A. About cross section for high-energy muon bremsstrahlung. *CERN Document Server* https://cds.cern.ch/record/288828/files/MEPHI-024-95.pdf (1995).
69. Sandrock, A. & Rhode, W. Coulomb corrections to the bremsstrahlung and electron pair production cross section of high-energy muons on extended nuclei. Preprint at https://arxiv.org/abs/1807.08475 (2018).
70. Melis, K. et al. (on behalf of the KM3NeT Collaboration) in *Proc. 35th International Cosmic Ray Conference* 1059 (SISSA, 2017).
71. Ageron, M. et al. (ANTARES Collaboration), ANTARES: the first undersea neutrino telescope. *Nucl. Instrum. Methods Phys. Res. A* **656**, 11–38 (2011).
72. Albert, A. et al. (ANTARES Collaboration), Monte Carlo simulations for the ANTARES underwater neutrino telescope. *J. Cosmol. Astropart. Phys.* **01**, 064 (2021).
73. Melis, K., Heijboer, A. & De Jong, M. (on behalf of the KM3NeT Collaboration) in *Proc. 35th International Cosmic Ray Conference* 950 (SISSA, 2017).
74. Viola, S. et al. (on behalf of the KM3NeT Collaboration) in *Proc. 34th International Cosmic Ray Conference* 1169 (SISSA, 2015).
75. Gatius Oliver, C. et al. (on behalf of the KM3NeT Collaboration) in *Proc. 38th International Cosmic Ray Conference* 1033 (SISSA, 2023).
76. Aiello, S. First observation of the cosmic ray shadow of the Moon and the Sun with KM3NeT/ORCA. *Eur. Phys. J. C* **83**, 344 (2023).
77. Abreu, P. et al. (Pierre Auger Collaboration), The energy spectrum of cosmic rays beyond the turn-down around 10^{17} eV as measured with the surface detector of the Pierre Auger Observatory. *Eur. Phys. J. C* **81**, 966 (2021).
78. Abbasi, R. U. et al. (Telescope Array Collaboration), The energy spectrum of cosmic rays measured by the Telescope Array using 10 years of fluorescence detector data. *Astropart. Phys.* **151**, 102864 (2023).
79. Klimushin, S. I., Bugaev, E. V. & Sokalski, I. A. Parametrization of atmospheric muon angular flux underwater. *Phys. Rev. D* **64**, 014016 (2001).
80. Fedynitch, A. et al. in *Proc. 18th International Symposium on Very High Energy Cosmic Ray Interactions* 08001 (EDP Sciences, 2015).
81. Fedynitch, A. et al. Hadronic interaction model SIBYLL 2.3c and inclusive lepton fluxes. *Phys. Rev. D* **100**, 103018 (2019).
82. Gaisser, T. K. Spectrum of cosmic-ray nucleons, kaon production, and the atmospheric muon charge ratio. *Astropart. Phys.* **35**, 801–806 (2012).
83. Benzke, M. et al. Prompt neutrinos from atmospheric charm in the general-mass variable-flavor-number scheme. *J. High Energy Phys.* **2017**, 21 (2017).
84. Gorski, K. M. et al. HEALPix: a framework for high-resolution discretization and fast analysis of data distributed on the sphere. *Astrophys. J.* **622**, 759–771 (2005).
85. Massaro, F. et al. The WISE gamma-ray strip parameterization: the nature of the gamma-ray active galactic nuclei of uncertain type. *Astrophys. J.* **750**, 138 (2012).
86. Plavin, A. V. et al. Growing evidence for high-energy neutrinos originating in radio blazars. *Mon. Not. R. Astron. Soc.* **523**, 1799–1808 (2023).
87. Aab, A. et al. (Pierre Auger Collaboration), Limits on point-like sources of ultra-high-energy neutrinos with the Pierre Auger Observatory. *J. Cosmol. Astropart. Phys.* **11**, 004 (2019).
88. Meier, M. (on behalf of the IceCube Collaboration), Recent cosmogenic neutrino search results with IceCube and prospects with IceCube-Gen2. Preprint at https://arxiv.org/abs/2409.01740 (2024).
89. Aiello, S. et al. (KM3NeT Collaboration), Data for the KM3-202313A high energy event observation. *Zenodo* https://doi.org/10.5281/zenodo.13366058 (2025).
90. EMODnet Bathymetry Consortium, EMODnet Digital Bathymetry (DTM 2022). https://doi.org/10.12770/ff3aff8a-cff1-44a3-a2c8-1910bf109f85 (2022).
91. Muller, R. et al. (on behalf of the KM3NeT Collaboration) in *Proc. 38th International Cosmic Ray Conference* 1018 (SISSA, 2023).
92. Aiello, S. et al. (KM3NeT Collaboration), Search for neutrino emission from GRB 221009A using the KM3NeT ARCA and ORCA detectors. *J. Cosmol. Astropart. Phys.* **08**, 006 (2024).
93. IceCube Collaboration, All-sky point-source IceCube data: years 2008–2018. Harvard Dataverse, V1, UNF:6:BI1pJQ7rl8vTfAwxAIxClg==. https://doi.org/10.7910/DVN/VKL316 (2024).
94. Albert, A. et al. (ANTARES Collaboration), First all-flavor neutrino pointlike source search with the ANTARES neutrino telescope. *Phys. Rev. D* **96**, 082001 (2017).
95. Barbano, E. et al. in *Proc. 38th International Cosmic Ray Conference* 1540 (SISSA, 2023).
96. Lamoureux, M. & de Wasseige, G. Multi-observations multi-energy neutrino transient analysis. *Zenodo* https://doi.org/10.5281/zenodo.13208670 (2024).

Acknowledgements The KM3NeT Collaboration acknowledges the generous hospitality and support of the Laboratori Nazionali del Sud, Italy. We acknowledge the financial support of: KM3NeT-INFRADEV2 project, financed by the European Union Horizon Europe Research and Innovation Programme under grant agreement no. 101079679; Funds for Scientific Research (FRS-FNRS); Francqui Foundation; Belgian American Educational Foundation; Czech Science Foundation (GAČR 24-12702S); Agence Nationale de la Recherche (contract ANR-15-CE31-0020); Centre National de la Recherche Scientifique (CNRS); Commission Européenne (FEDER fund and Marie Curie Program); LabEx UnivEarthS (ANR-10-LABX-0023 and ANR-18-IDEX-0001), Paris Île-de-France Region, Normandy Region (Alpha, Blue-waves and Neptune), France; the Provence-Alpes-Côte d'Azur Delegation for Research and Innovation (DRARI), the Provence-Alpes-Côte d'Azur region, the Bouches-du-Rhône Departmental Council, the Metropolis of Aix-Marseille Provence and the City of Marseille through the CPER 2021-2027 NEUMED project; the CNRS Institut National de Physique Nucléaire et de Physique des Particules (IN2P3); Shota Rustaveli National Science Foundation of Georgia (SRNSFG, FR-22-13708), Georgia. This work is part of the MuSES project, which has received financing from the European Research Council (ERC) under the European Union's Horizon 2020 research and innovation programme (grant agreement no. 101142396). This work was supported by the European Research Council, ERC Starting grant MessMapp, under contract no. 949555; the General Secretariat of Research and Innovation (GSRI), Greece; Istituto Nazionale di Fisica Nucleare (INFN) and Ministero dell'Università e della Ricerca (MUR), through PRIN 2022 programme (grant PANTHEON 2022E2J4RK, Next Generation EU) and PON R&I programme (Avviso n. 424 del 28 febbraio 2018, Progetto PACK-PIR01 00021), Italy; IDMAR project Po-Fesr Sicilian Region az. 1.5.1. A.D.B., W.I.I., M.B., A.N., G.P., I.C.R. and A.Sim. have been supported by the Italian Ministero dell'Università e della Ricerca (MUR), Progetto CIR01 00021 (Avviso n. 2595 del 24 dicembre 2019); KM3NeT4RR MUR Project National Recovery and Resilience Plan (NRRP), Mission 4 Component 2 Investment 3.1, financed by the European Union - NextGenerationEU, CUP I57G21000040001, Concession Decree MUR no. n. Prot. 123 del 21/06/2022; Ministry of Higher Education, Scientific Research and Innovation, Morocco, and the Arab Fund for Economic and Social Development, Kuwait; Nederlandse organisatie voor Wetenschappelijk Onderzoek (NWO), the Netherlands; the grant 'AstroCeNT: Particle Astrophysics Science and Technology Centre', carried out within the International Research Agendas programme of the Foundation for Polish Science financed by the European Union under the European Regional Development Fund; the programme 'Excellence initiative-research university' for the AGH University in Krakow; the ARTIQ project: UMO-2021/01/2/ST6/00004 and ARTIQ/0004/2021; Ministry of Research, Innovation and Digitalisation, Romania; Slovak Research and Development Agency under contract no. APVV-22-0413; Ministry of Education, Research, Development and Youth of the Slovak Republic; MCIN for PID2021-124591NB-C41, -C42, -C43 and PDC2023-145913-I00 financed by MCIN/AEI/10.13039/501100011033 and by 'ERDF A way of making Europe', for ASFAE/2022/014 and ASFAE/2022 /023 with funding from the EU NextGenerationEU (PRTR-C17.I01) and Generalitat Valenciana, for grant AST22_6.2 with funding from Consejería de Universidad, Investigación e Innovación and Gobierno de España and European Union - NextGenerationEU, for CSIC-INFRA23013 and for CNS2023-144099, Generalitat Valenciana for CIDEGENT/2018/034, /2019/043, /2020/049, /2021/23, for CIDEIG/2023/20, for CIPROM/2023/51 and for GRISOLIAP/2021/192 and EU for MSC/101025085, Spain; Khalifa University internal grants (ESIG-2023-008 and RIG-2023-070), United Arab Emirates; the European Union's Horizon 2020 research and innovation programme (ChETEC-INFRA - project no. 101008324).

Author contributions The KM3NeT research infrastructure is being built, operated and maintained by the KM3NeT Collaboration. Authors contributed to the design, construction, deployment and operation of the detector, as well as to the data taking, detector calibration, development of the software, data processing, Monte Carlo simulations and various analyses required for this work. The final manuscript was reviewed and approved by all authors.

Competing interests The authors declare no competing interests.

Additional information

Supplementary information The online version contains supplementary material available at https://doi.org/10.1038/s41586-024-08543-1.

Correspondence and requests for materials should be addressed to The KM3NeT Collaboration.

Peer review information *Nature* thanks the anonymous reviewers for their contribution to the peer review of this work.

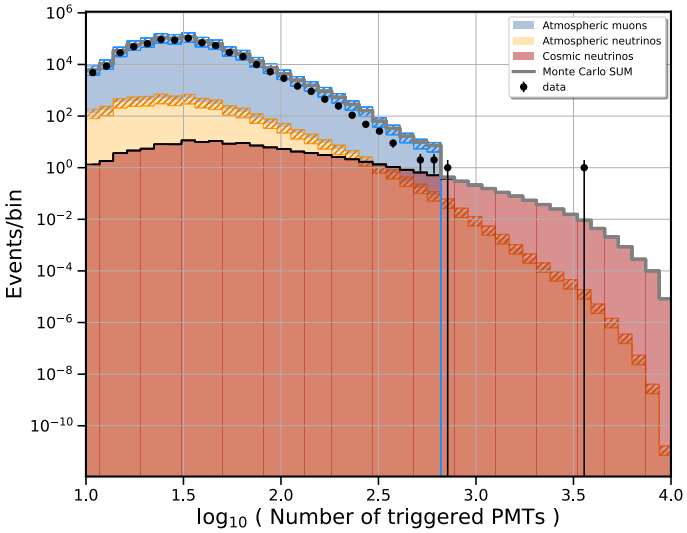

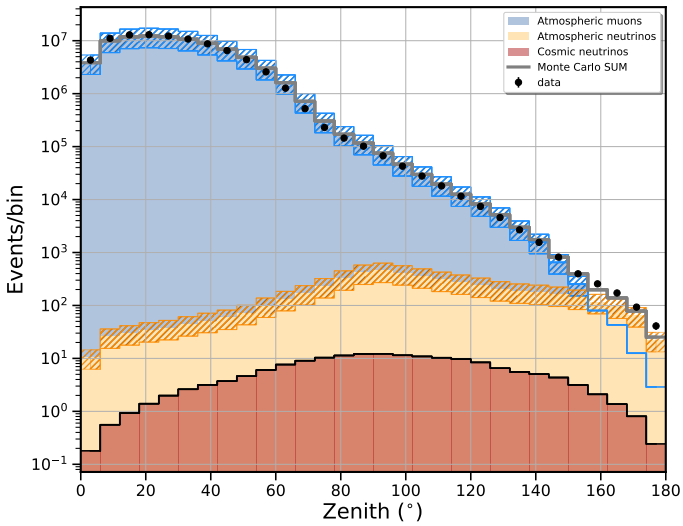

Extended Data Fig. 1 | Comparison between data and Monte Carlo simulations. The distribution of the $\mathcal{N}_{\text{trig}}^{\text{PMT}}$ observable is shown on the left and the reconstructed zenith angle on the right. Simulated atmospheric muons are shown in blue and atmospheric neutrinos are shown in yellow. A 40% systematic uncertainty on their normalization is also included in the histograms. The expected distribution for a cosmic neutrino flux described by the best fit from the IceCube Northern Sky Tracks[5] is shown for comparison in red.

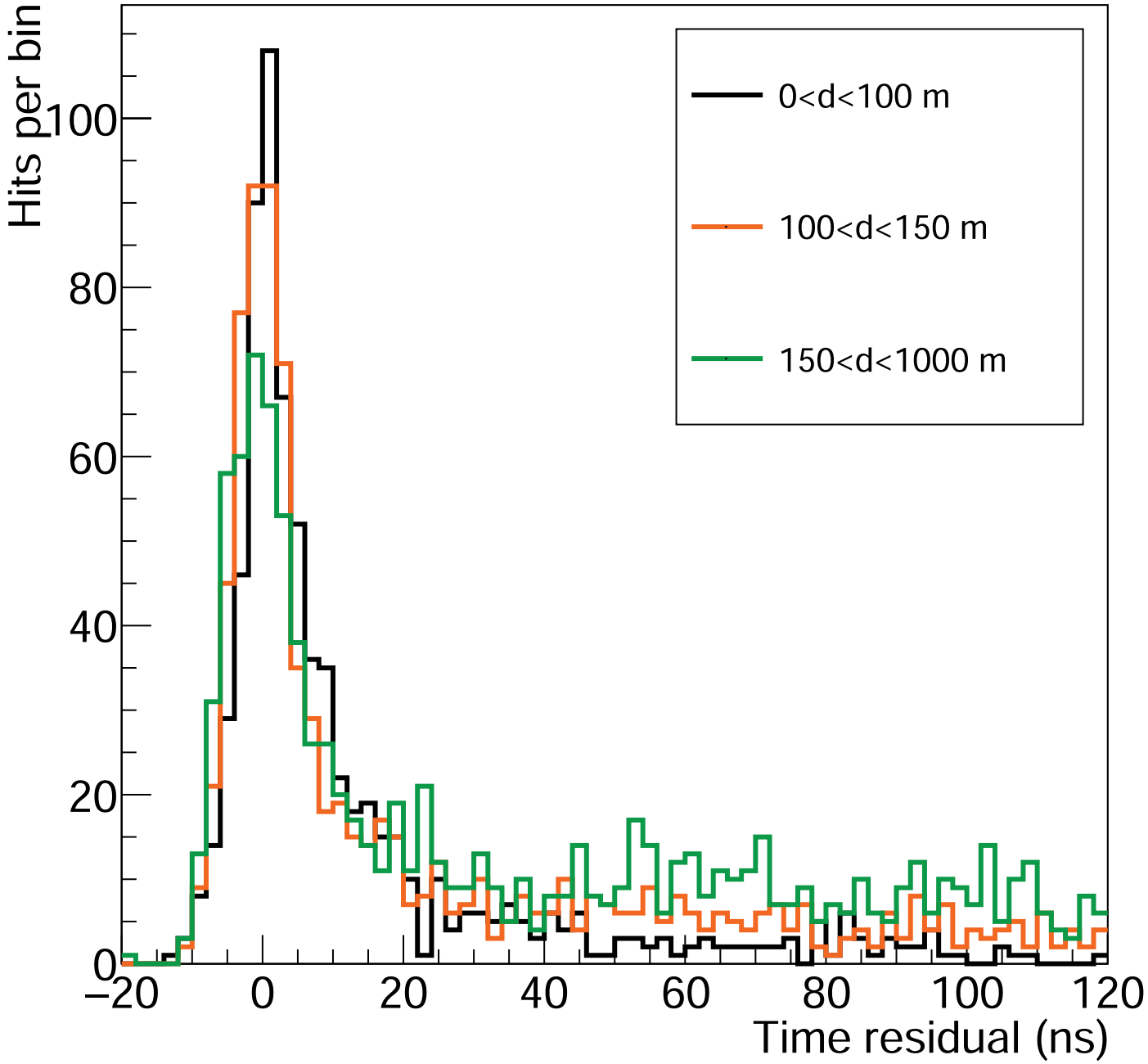

Extended Data Fig. 2 | Time residual distribution. The time residual is defined as the difference between the time of arrival of the detected photons in the event and the expected time from Cherenkov radiation, induced by a relativistic muon. The distributions at various distances *d* from the track are shown, with coloured lines as indicated in the legend. In this figure, only the first hit on each PMT is used.

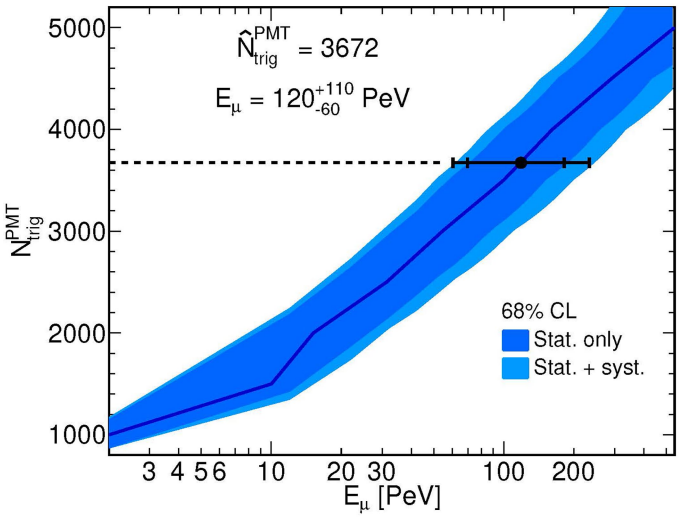

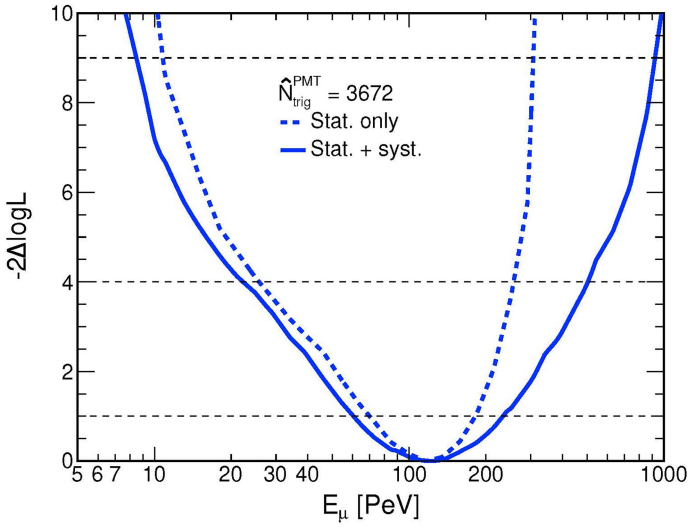

Extended Data Fig. 3 | Energy measurement. Left, the true muon energy E_μ maximizing the likelihood value for a given N^{PMT}_{trig} is shown as a blue line. The blue bands show the 1σ confidence level, computed from the likelihood distribution using Wilks' theorem[13]: in dark blue when only statistical uncertainties are considered, in light blue when systematic uncertainties are also included. The observed value $\hat{N}^{PMT}_{trig} = 3{,}672$ corresponds to the horizontal dashed line. The resulting muon energy estimate is also reported (including systematic uncertainties). Right, log-likelihood profile for $\hat{N}^{PMT}_{trig} = 3{,}672$: the dashed blue curve represents the results when only the statistical uncertainty is considered, whereas the solid blue curve shows the results when including systematic uncertainties. The dashed horizontal lines represent the 1σ, 2σ and 3σ confidence level according to Wilks' theorem.

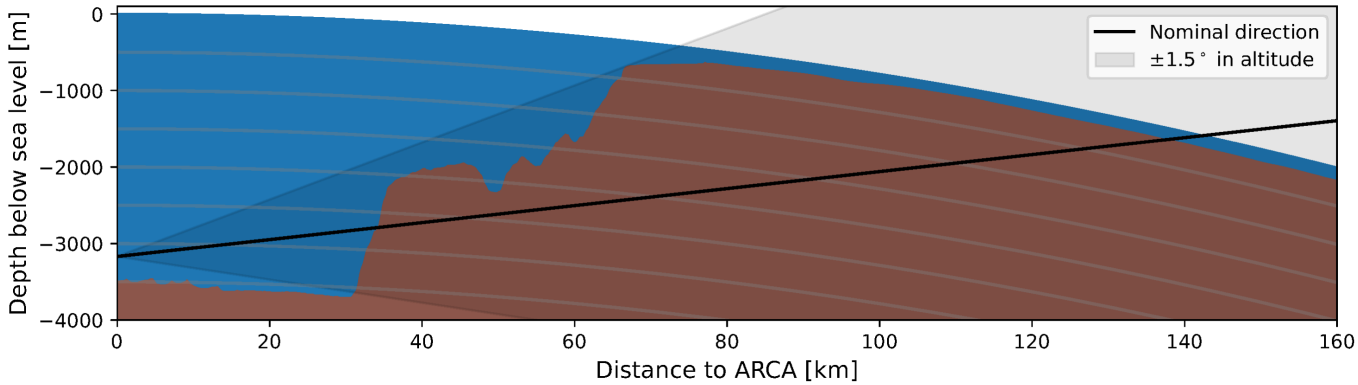

Extended Data Fig. 4 | Illustration of the topography. Using bathymetric data from EMODnet[90], a sectional view along the incoming direction and position of the event is shown, with the sea shown in blue and the seabed and the rock beneath in brown. The *x* axis indicates the total distance from the ARCA site and the *y* axis and grey lines represent the depth with respect to the sea level. The shaded area shows the effect of a variation of ±1.5° in the direction reconstruction, corresponding to the 68% error region from the evaluation of systematic uncertainties.

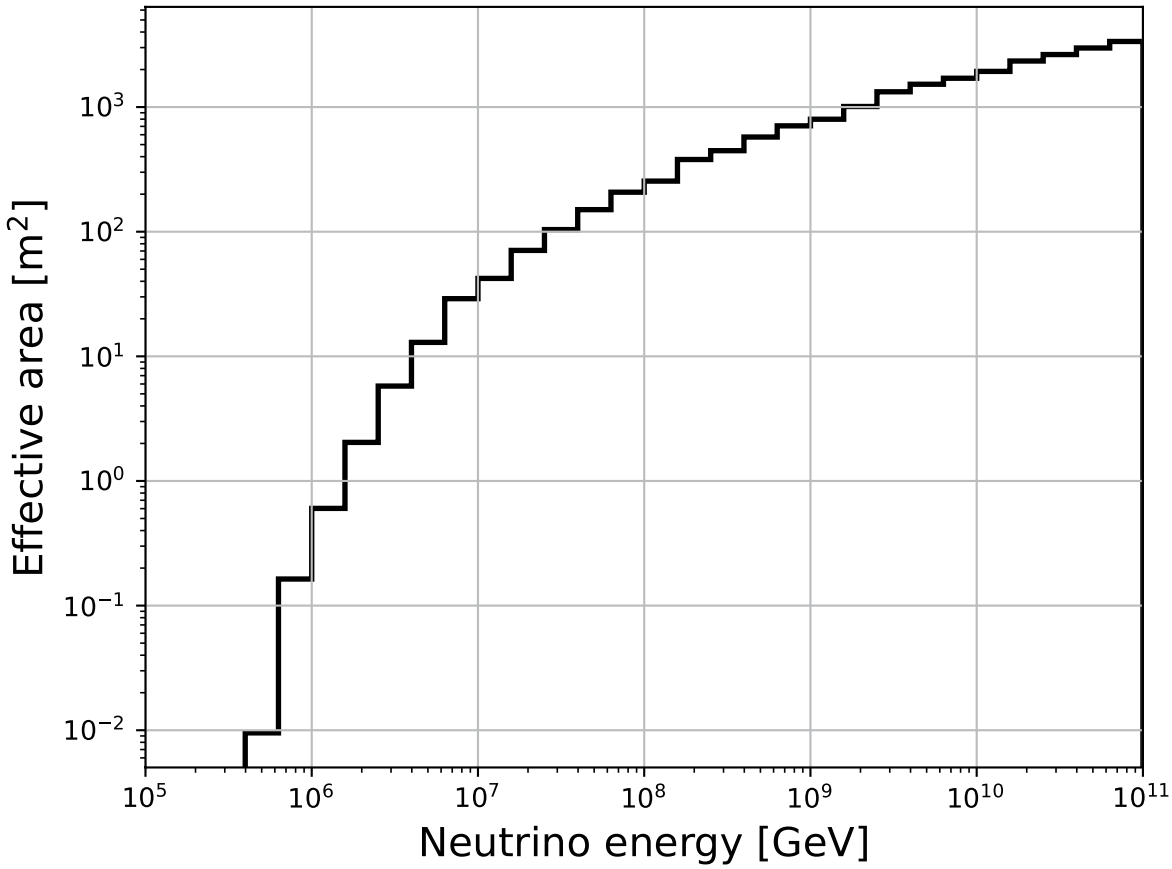

Extended Data Fig. 5 | All-flavour sky-averaged effective area for KM3NeT/ARCA. The area in the 21 detection line configuration is shown as a function of neutrino energy. This effective area is computed after applying the event selection described in the text and is averaged between neutrinos and antineutrinos.

Extended Data Table 1 | Datasets and methods used in the searches for a cosmic point-like neutrino source in the direction of KM3-230213A. Refs. 91–93

Dataset				Method	
Detector	Covered Period dd/mm/yyyy	Livetime [days]	Type of Data	Analysis Approach	Radius [deg]
ARCA6-21	12/05/2021 - 11/09/2023	640	offline	binned likelihood [91]	3
ORCA6-18	11/02/2020 - 31/08/2023	1005	offline	ON/OFF [92]	4
ORCA18-23	01/09/2023 - 29/07/2024	126	online	ON/OFF [92]	4
ANTARES	29/01/2007 - 31/12/2017	3125	public	unbinned likelihood	3
IceCube	06/04/2008 - 08/07/2018	3577	public [93]	unbinned likelihood	3

For each investigated dataset, the corresponding detector, covered period, livetime, type of data, analysis method and radius of the circular inspected region centred at the location of KM3-230213A are reported. The 'Type of data' column refers to fully calibrated data (offline) or using preliminary calibrations (online). KM3-230213A was removed from the ARCA6-21 dataset. The ANTARES dataset is taken from https://antares.in2p3.fr/data/data-set-for-the-2007-2017-antares-search-for-cosmic-neutrino-point-sources/; it is analysed with a method from ref. 94, with the difference that no energy information is considered in the likelihood and that a two-dimensional Gaussian is used to describe the signal spatial distribution. For the IceCube data, the IceCubePy framework[95] is used, without including the energy information in the likelihood.

Extended Data Table 2 | Results of the searches for a cosmic point-like neutrino source in the direction of KM3-230213A

Dataset	$n_{\rm sig}$	$-\log_{10}(p\text{-value})$	Flux Upper Limit $[\mathrm{GeV}^{-1}\mathrm{cm}^{-2}\mathrm{s}^{-1}]$	(RA, Dec) [deg, deg]	Distance [deg]	P-value
ARCA6-21	0.4	0.044	1.8×10^{-8}	(94.3, −7.8)	0.0	-
	1.3	1.308	1.9×10^{-8}	(96.7, −6.8)	2.6	0.44
ORCA6-18	0	-	2.1×10^{-7}	-	-	-
ORCA18-23	0	-	2.3×10^{-6}	-	-	-
ORCA-combined	-	-	2.0×10^{-7}	-	-	-
ANTARES	0	-	1.1×10^{-8}	(94.3, −7.8)	0.0	-
	1.9	1.936	1.7×10^{-8}	(94.4, −5.3)	2.5	0.53
IceCube	1.4	0.327	1.2×10^{-9}	(94.3, −7.8)	0.0	-
	15.1	3.782	6.3×10^{-9}	(93.9, −10.1)	2.4	0.07

For each investigated dataset, the corresponding results are shown in terms of the number of signal events (either observed in the ON region or fitted by the likelihood maximization), pre-trial P-value and 90% confidence level upper limit on the one-flavour neutrino flux normalization at 1GeV, $\Phi^{1\mathrm{GeV}}_{\nu+\bar{\nu}}$, assuming a neutrino spectrum of $\Phi_{\nu+\bar{\nu}}(E) = \Phi^{1\mathrm{GeV}}_{\nu+\bar{\nu}}(E(\mathrm{GeV}))^{-2}$. In the case of likelihood scan (ARCA6-21, ANTARES, IceCube), results are given both for the location of KM3-230213A (RA = 94.3°, dec. = −7.8°) and for the most significant direction in the inspected region, together with equatorial coordinates and distance from the event. For the most significant direction, the post-trial P-value (P-value) is also provided. The fifth row reports the combined limit of the two ORCA analyses obtained with the dedicated framework MOMENTA[96].

Extended Data Table 3 | Potential blazars pinpointed using the strategies described in Methods, located within 68%, 90% and 99% error regions around KM3-230213A

Source	RA [deg]	Dec [deg]	Dist [deg]	Name	Association	Methods
		R(68%)				
#1	94.263708	−8.373833	0.57	NVSS J061703−082225	WISE J061702.95−082229.5, 1RXS J061702.4−082229	(1)
#2	94.0571	−6.8983	0.94	4FGL J0616.2−0653		(4)
		R(90%)				
#3	95.741858	−6.94777	1.66	RFC J0622−0656		(2)
#4	96.230542	−7.593528	1.92	NVSS J062455−073536	4FGL J0624.8−0735	(4)
#5	94.586114	−9.907146	2.12	RFC J0618−0954		(2)
		R(99%)				
#6	91.998747	−8.58055	2.41	RFC J0607−0834	4FGL J0608.0−0835, 5BZQ J0607−0834	(1, 2, 3, 4)
#7	92.416542	−6.251611	2.43	CRATES J0609−0615	5BZQ J0609−0615, WISEA J060939.96−061506.0	(3)
#8	91.681443	−7.408397	2.63	RFC J0606−0724	5BZQ J0606−0724	(1, 2, 3)
#9	94.174198	−10.685682	2.88	RFC J0616−1041	WISE J061641.80−104108.4, PMN J0616−1040, 4FGL J0616.7−1049	(1, 2, 4)
#10	91.666542	−6.572528	2.89	NVSS J060639−063421	WISEA J060640.00−063419.6, 1eRASS J060640.2−063424	(1)
#11	91.359125	−7.992167	2.92	CRATES J0605−0759	WISEA J060526.16−075931.7, RFC J0605−0759, 1eRASS J060527.0−075925	(1)
#12	91.288708	−7.963250	2.99	NVSS J060509−075747	WISEA J060509.22−075747.1, 1eRASS J060509.0−075739	(1)

Their positions are given in equatorial (J2000) coordinates. Sources are numbered according to their distance from KM3-230213A, corresponding to the source listed in the 'Name' column. The 'Association' column includes catalogued objects at other wavelengths that are associated with this source. The last column indicates the method that led to the identification of the source.